applied sciences

MDPI

Review

Amplified Spontaneous Emission and Lasing in Lead Halide Perovskites: State of the Art and Perspectives

Maria Luisa De Giorgi and Marco Anni *

Dipartimento di Matematica e Fisica "Ennio De Giorgi", Università del Salento, Via per Arnesano, 73100 Lecce, Italy; marialuisa.degiorgi@unisalento.it

* Correspondence: marco.anni@unisalento.it; Tel.: +39-0832-297540

Received: 9 October 2019; Accepted: 24 October 2019; Published: 29 October 2019

Abstract: Lead halide perovskites are currently receiving increasing attention due to their potential to combine easy active layers fabrication, tunable electronic and optical properties with promising performance of optoelectronic and photonic device prototypes. In this paper, we review the main development steps and the current state of the art of the research on lead halide perovskites amplified spontaneous emission and on optically pumped lasers exploiting them as active materials.

Keywords: lead halide perovskite; thin film; nanocrystal; optical gain; amplified spontaneous emission; laser

1. Introduction

In the frame of developing novel active materials for electronic, optoelectronic and photonic devices, lead halide perovskites are currently receiving great attention due to their capability to combine an easy realization procedure, widely tunable electronic properties and promising performance as active materials for a wide range of devices. In particular, perovskite-based solar cells demonstrated an impressively fast power conversion efficiency increase, from 3.8% in TiO_2 sensitized photoelectrochemical cells [1], to the recent record value of 25.2% [2] in thin film solar cells.

Lead halide perovskites also showed interesting photoluminescence (PL) and electroluminescence properties, which stimulated the research in light emitting devices, such as light emitting diodes (LEDs) [3].

Moreover, also the first reports of room temperature amplified spontaneous emission (ASE) and high optical gain both in solution processed bulk polycrystalline thin films [4] and in perovskite nanocrystals (NCs) thin films [5] strongly stimulated further research aiming to develop laser devices exploiting lead halide perovskites as active materials.

In addition, in this case, the development was very fast, leading to the first evidence of optically pumped lasing in microcavities [6] basically simultaneously to the first report on ASE, and to the first report of single mode lasing under continuous wave excitation [7] only three years later.

Beyond these breakthroughs, wide research activity allowed many groups to propose approaches to improve the ASE and lasing properties addressing many aspects, like threshold reduction, wavelength range engineering, lasing cavity geometry and stability improvement.

In this paper, we will review the main developments in the field of halide perovskite for lasers application and we will describe the state of the art and the future development perspectives.

We will initially describe the main results on the investigation of ASE in perovskites thin film, we will then illustrate the developments and the state of the art of optically pumped lasers exploiting lead halide perovskites as active materials, and finally we will discuss the application perspectives to electrically and optically pumped laser devices.

2. Amplified Spontaneous Emission

The first property required for a candidate active material for lasers is the capability to show optical gain, leading to light amplification during its propagation in the material. A common experiment to observe the presence of optical gain is the measurement of the excitation density dependence of the PL spectra. When the excitation density is high enough to make optical gain higher than the propagation losses a stimulated emission band appears in the spectral region of highest gain, most of the time due to amplification of the spontaneous emission, and thus named amplified spontaneous emission (ASE). The experiments to observe and quantitatively characterize the ASE are relatively simple and are thus often performed as initial step in the investigation of the properties of novel materials for lasers applications. In this section, we will review the main results reported in the literature on the ASE properties of lead halide perovskites thin films starting from bulk polycrystalline thin films and then moving to nanocrystals thin films.

2.1. Perovskites Bulk Polycrystalline Thin Films

The first evidence of optical gain in lead halide perovskites were reported back in 2004 by Kondo et al. [8,9] in microcrystalline films of $CsPbCl_3$, obtained by recrystallization from the amorphous phase, showing evidence for the presence of ASE at low temperature (up to about 180 K). The same group also later demonstrated room temperature ASE in $CsPbCl_3$ [10] and in $CsPbBr_3$ [11].

These initial results however remained basically isolated, probably due to the complex realization procedure of the active materials, and the interest in lead halide perovskites for lasing application strongly increased only after the first demonstration of room temperature optical gain and ASE in organic-inorganic solution processed methylammonium (CH_3NH_3, MA) lead halides $MAPbX_3$ (where X = Cl, Br, I) films by Xing et al. [4]. The authors investigated the excitation density dependence of the PL spectra of $MAPbI_3$ films under 150 fs pulses pumping at 600 nm, observing the typical $MAPbI_3$ spontaneous emission spectra at low excitation density, and the progressive appearance of a narrow band at 788 nm as the excitation density increased (see Figure 1a). The lineshape variation also resulted in a superlinear intensity increase and in a clear spectral narrowing, allowing to ascribe these results to the appearance of ASE, above a threshold of 12 μJcm^{-2}. A remarkable ASE operational stability was also reported, with almost stable ASE intensity during continuous laser pumping at 18 μJcm^{-2} in vacuum up to 9×10^7 laser shots (see Figure 1b). Finally, complete coverage of the visible range was obtained by changing the chemical composition through halide substitution. In particular, by using either mixtures of bromides and iodides or chlorides and iodides, a bandgap (and ASE peak wavelength) tuning from 390 nm to 790 nm was demonstrated (see Figure 1c).

The combination of easy deposition from solution, low ASE threshold and high stability strongly stimulated further research in order to optimize the ASE properties.

The initial works focused on a physical approach, based on the optimization of the waveguide structure, in order to improve the light amplification efficiency of the active layer.

A first example of this approach was reported by Stranks et al. [12] that obtained ASE under 5 nanoseconds pumping at 532 nm in $MAPbI_3$ thin films sandwiched between two 50 nm-thick polymethylmethacrylate (PMMA) layers and two cholesteric liquid crystals (CLC) reflectors, with a minimum threshold of only 7.6 μJcm^{-2}. This result was ascribed to the increase of the optical path length in the medium due to reflection and redirection toward the active layer by the CLC layers of the emission that propagates along the out-of-plane and oblique paths.

Another approach is the realization of perovskite-PMMA bilayers, as reported by Li et al. [13] with $MAPbBr_3$ active films. The perovskite layer was realized by a two step sequential deposition process, and was then coated with a top PMMA layer deposited by spin coating. The authors observed that the PMMA coated film showed higher PL intensity, slower PL relaxation dynamics, and ASE threshold about 2.2 times lower. These results were ascribed in part to the passivation of defects in the perovskite top surface, accounting for the higher PL intensity, the slower PL relaxation and for about 20% of the ASE threshold decrease. The remaining ASE threshold decrease was

instead ascribed to improved waveguiding, allowed by the realization of an almost symmetric glass-perovskite-PMMA waveguide that results in higher mode confinement in the perovskite layer with respect to the asymmetric glass-perovskite one, as also demonstrated some years before in organic polymers amplifying waveguides [14]. A similar approach has also been recently reported in $MAPbI_3$ films, observing a threshold reduction of about 1.5 times, due to the deposition of the top PMMA layer, and a strong increase of the ASE intensity (up to 13.9 times) due to the further addition of a PMMA-gold nanorod layer, and ascribed to plasmonic effects [15].

Several other experiments instead exploited the degrees of freedom of the active layer deposition from solution, thus modifying either the solutions properties or the deposition method in order to optimize the film morphology and optical properties.

For example enhanced ASE properties were demonstrated in $MAPbI_3$ thin films with controlled morphology [16]. The films were realized by a two step sequential deposition process, by initially depositing a PbI layer from solution, and then dipping the film in a solution of MAI. The variation of the solvents used to dissolve PbI allowed changing the PbI film morphology and, as a consequence, the final $MAPbI_3$ one. A minimum ASE threshold of 54.1 μJcm^{-2}, under 5 ns pumping at 500 nm, was reached in the film with the lowest roughness and grain size, due to the combination of maximum gain and minimum waveguide losses.

The role of the micromorphology and of the crystalline grain size was also investigated in green emitting $MAPbBr_3$ films by comparing the optical amplification properties of films deposited with two different methods: simple spin coating of a precursor solution and two step antisolvent deposition [17]. In the last approach the precursor solution is spin coated on the substrate and dripped with an antisolvent in order to increase the evaporation rate and to decrease the crystalline grain size, leading to the so-called "nano-crystal pinning" (NCP). The investigation of the film morphology allowed to observe, in the as-cast film, the presence of isolated plate-like microcrystals with a widely distributed size from several μm to nearly 100 μm. On the contrary the NCP film showed smooth and uniform surface due to better coverage and smaller microcrystals size (below 100 nm). Moreover the NCP film demonstrated a photoluminescence quantum yield (PLQY) 2.4 times larger and an ASE threshold about 1.7 times smaller than the as-cast film.

The same approach was also used in order to optimize the ASE properties of $MAPbBr_3$ films, as a preliminary step for the realization of Distributed Feedback (DFB) lasers [18], resulting in comparable ASE threshold values of the NCP film.

Another example of the role of the solution on the film morphology and on its optical properties was obtained by the development of a modified antisolvent deposition method for $MAPbI_3$ [19]. In particular the authors demonstrated that the presence of organic molecules additives to the antisolvent reduces the ASE threshold up to 4 times, down to a minimum value of 600 μJcm^{-2}, under 1 ns pumping at 533 nm. This result is due to the localization of the additive molecules at the grain boundaries of the perovskite film, thus passivating non radiative recombination centers at the grain boundary surface.

A further approach to improve the active layer morphology was demonstrated in $MAPbI_{3-x}Cl_x$ films deposited by double spin coating from a precursor solution [20]. In this case, the sample realized by standard spin coating did not show ASE; it was instead present in the sample deposited by double spin coating with a threshold of 50 μJcm^{-2} under 880 ps at 337 nm pumping. This difference was ascribed to a higher surface coverage of the sample obtained by double spin coating, and thus better waveguiding properties.

All these results evidence the possibility to realize $MAPbX_3$ films, showing promising low ASE threshold values and several possible optimization degrees of freedom. Anyway the applicative perspectives of these materials are currently limited by the known poor stability to light irradiation, heating and moisture exposure. This issue is relevant for all the possible device application of perovskites, including solar cells, thus a large research is running in order to improve the active materials and the devices stability.

In the particular case of laser applications it is important to observe that, in order to reach the population inversion, the optical pumping regime of the active layers is typically very strong. Moreover, in order to realize low cost devices, either optically or electrically pumped, it is necessary to use long excitation pulses (at least in the nanosecond scale) or, hopefully, continuous wave excitation thus requiring stable materials against heating.

A powerful strategy to improve the active layer stability is the chemical engineering of the active material, aiming to exclude less stable components and, in particular, to replace MA with more stable cations. For example it was demonstrated that formamidinium ($CH(NH_2)_2$, FA)-based perovskites and, in particular, in $FAPbI_3$, show low threshold ASE and almost constant ASE intensity during continuous under 5 ns pumping at 532 nm pumping up to at least 2×10^5 pulses (while, under the same pumping conditions, the $MAPbI_3$ ASE intensity drops to only 9% of the initial value) [21].

Another promising class of materials with improved stability are fully inorganic compounds in which the organic cation is substituted by an inorganic specie (typically Cs).

The first results on ASE in fully inorganic lead halide perovskites were obtained by De Giorgi et al. [22] demonstrating ASE in $CsPbBr_3$ films at cryogenic temperatures (up to 150 K) with a minimum threshold of 26 μJcm^{-2} at 10 K, under 3 ns pumping at 337 nm. The investigation of the temperature dependence of the PL spectra allowed to demonstrate that the ASE properties are strongly affected by the presence of defects and by their energy distribution, causing the presence of thermally activated exciton trapping or detrapping.

Room temperature ASE was later demonstrated in $CsPbBr_3$ films deposited by one step coevaporation of CsBr and $PbBr_2$, also showing unchanged ASE threshold after 10 days of storage in air and almost constant ASE intensity during exposure to 2×10^5 5.5 nanosecond pulses at 353 nm [23].

More recently, Pourdavoud et al. [24] succeeded in obtaining room temperature ASE in $CsPbBr_3$ films deposited from solution thanks to high temperature and pressure induced recrystallization of pristine films not showing ASE. This approach strongly modified both the morphology and the optical properties of the active films, reducing the roughness from 23.8 nm to only 0.5 nm and increasing the PLQY from 43% to 53%, thus allowing to observe room temperature ASE with a threshold of 12.5 μJcm^{-2}, under 300 ps pumping at 355 nm.

A very recent breakthrough toward future application of lead halide perovskites to real lasers was reported by Brenner et al. [25] that demonstrated, for the first time, ASE under continuous wave optical excitation at 532 nm in the temperature range 80–120 K, with a minimum threshold of 400 Wcm^{-2} in a phase stable triple cation non stoichiometric $Cs_{0.1}(MA_{0.17}FA_{0.83})_{0.9}Pb_{0.84}(I_{0.84}Br_{0.16})_{2.68}$. At higher temperatures the active material degradation prevented to reach the ASE threshold. While apparently still far from the requirements of CW operations at room temperature, or at least in the temperature range accessible by Peltier cooling (T > 220 K), this result is really impressive if one considers that it was obtained only five years later than the first ASE demonstration under femtosecond pumping. In other classes of materials proposed as alternative to standard semiconductors for laser application, like II-VI nanocrystals, it was necessary to wait about 20 years to reach the same result [26] while organic conjugated molecules to date did not show CW lasing, even if the first evidence of ASE was obtained back in 1996 [27].

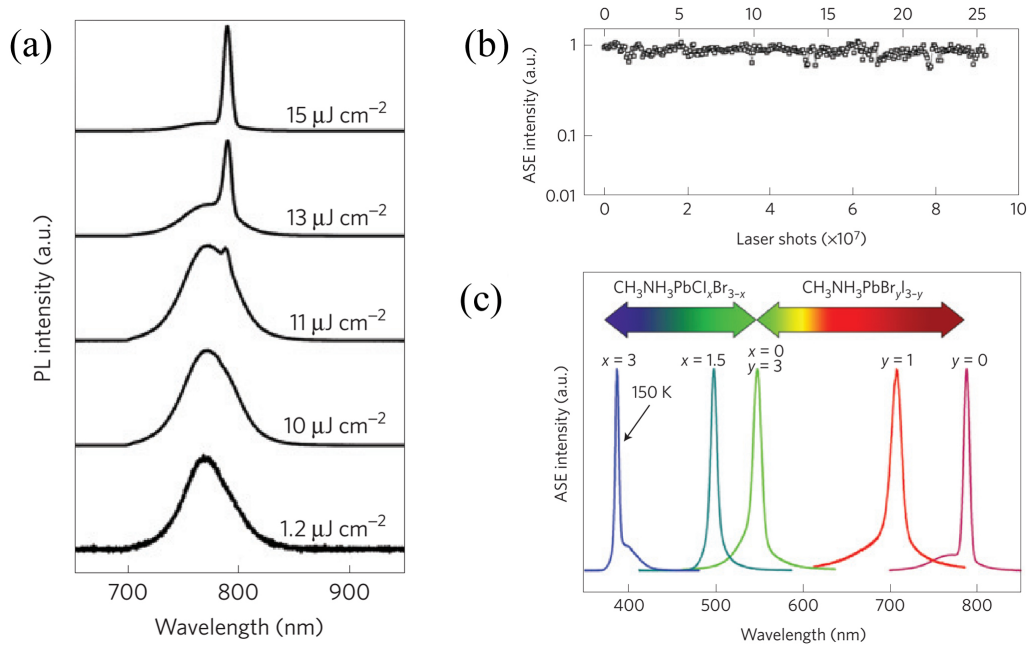

Figure 1. (**a**) Excitation density dependence of the PL spectra of a $MAPbI_3$ thin film, showing evidence for the appearance of the ASE band for excitation densities above 11 μJcm^{-2}. (**b**) $MAPbI_3$ ASE intensity operational stability under continuous pumping at 11 μJcm^{-2}. (**c**) ASE color tunability as a function of the film chemical composition. Adapted with permission from [4]. Nature Publishing group, 2014.

2.2. Perovskites Nanocrystals Thin Films

After their first realization by Protesescu et al. [28] fully inorganic $CsPbX_3$ nanocrystals rapidly emerged as extremely interesting active materials for application to photonic and optoelectronic devices, due to their narrow emission, high PLQY in solution and widely tunable emission color by chemical composition engineering (see Figure 2a,b). Only a few months later Yakunin et al. [5] demonstrated low threshold ASE and lasing at room temperature in $CsPbX_3$ nanocrystals thin films (see Figure 2c) both under femtosecond and nanosecond pulsed excitation. Moreover, full ASE tuning across the visible was obtained by compositional modulation (see Figure 2d). Almost simultaneously qualitatively similar results were also reported by Wang et al. [29], even if with higher ASE thresholds. The investigation of the temperature dependence of the PL and ASE properties in $CsPbBr_3$ NC films performed by Balena et al. [30] gave evidence of an ASE threshold reduction of about 20 times with respect to room temperature, down to 147 μJcm^{-2} at T = 10 K, under 3 ns pumping at 337 nm. Moreover, the ASE threshold temperature dependence clearly gave evidence of the presence of two critical temperatures (90 K and between 170 K and 190 K) at which the temperature dependence changes, ascribed to the thermally induced formation of nearly ordered orthorhombic subdomains within each nanocrystal.

Later several further works from the Kovalenko's group focused on the optimization of the NCs optical properties, by acting on their chemical composition or on the capping ligands one. In particular, $MAPbBr_3$ and $MAPbI_3$ NCs were synthesized by Vybornyi et al. [31], and $MAPbBr_3$ NCs films showed efficient ASE in the green, with a threshold about 2 times smaller that the $CsPbBr_3$ ones, but with much lower stability.

The chemical stability issue was instead addressed by Protesescu et al. [32] that reported $FAPbBr_3$ NCs, with a strongly improved stability during purification processes with respect to $CsPbBr_3$ and $MAPbBr_3$ and good ASE properties in the green. In a further experiment [33], $FAPbI_3$ and $FA_{0.1}Cs_{0.9}PbI_3$ NCs were synthesized, characterized by high PLQY and efficient ASE spanning the red and near infrared range. Efficient optical amplification in the nanosecond regime in $FAPbI_3$ NCs films was also demonstrated by Papagiorgis et al. [34] that obtained room temperature ASE with a

minimum threshold of 140 μJcm^{-2} in films annealed at 90°, under 4 ns pumping at 532 nm, while no ASE was observed in as-deposited films.

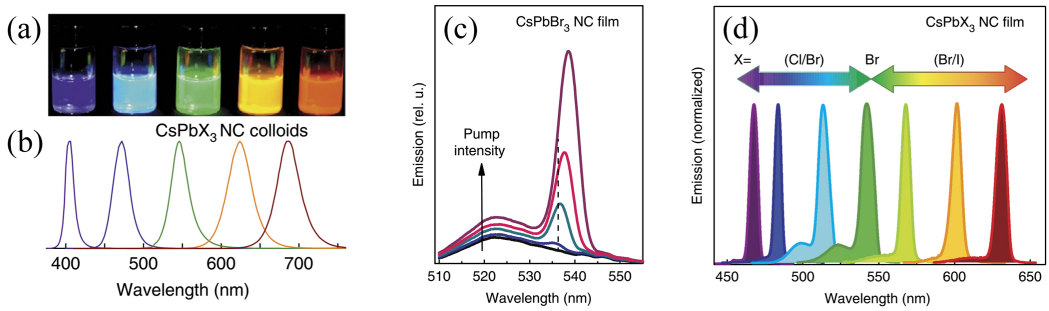

Figure 2. (**a**) Photograph of toluene dispersions of nanocrystals with four different chemical composition under UV light excitation. (**b**) PL spectra of the solutions in (**a**). (**c**) Excitation density dependence of the PL spectra of a $CsPbBr_3$ NCs thin film in the excitation range 3–25 μJcm^{-2}, showing evidence of the progressive appearance of the ASE band. (**d**) Spectral tunability of ASE by compositional modulation. Adapted with permission from [5]. Nature Publishing group, 2014.

Further improvements of the NCs stability during purification were obtained by Krieg et al. [35] that synthesized $CsPbBr_3$ NCs capped with zwitterionic long-chain molecules. These NCs demonstrated much higher long term stability and lower tendency to sintering, gave evidence of a PLQY in films comparable to the one in solution and of the retention of about 60% of the initial PLQY after 10 months of storage in ambient conditions. Excellent ASE properties were shown by a very low ASE threshold of only 2 μJcm^{-2}, under 100 fs pumping at 400 nm.

The possibility to improve the $CsPbBr_3$ NCs stability by acting on the ligand modification was also recently demonstrated by Yan et al. [36], who replaced oleic acid (OA) ligands with 2-hexyldecanoic acid (DA). The DA functionalized NCs showed an ASE threshold reduced of about 2 times with respect to OA NCs, even if much higher than the values found by Yakunin et al. [5].

Another approach to improve the NCs stability was instead proposed by Veldhuis et al. [37] that synthesized highly stable $MAPbBr_3$ NCs, improving the ligands passivation thanks to the addition of benzyl alcohol to the growth solution. Good ASE properties were shown by a reasonably low threshold of 14 μJcm^{-2}, under 150 fs pumping at 400 nm, while the stability was demonstrated by the absence of threshold variations during 4 months of storage under ambient condition and by the absence of photodegradation during continuous laser pumping up to 10^{11} femtosecond pulses.

A very interesting and recent step in the development of perovskite NCs with optimized optical properties was reported by Wang et al. [38], who developed a novel synthetic strategy, called intermediate monomer reservoir synthesis, allowing the growth of highly uniform, low defect and stable $CsPbBr_3$ nanorods with PLQY of 90% (see Figure 3a). A detailed comparison with $CsPbBr_3$ nanocubes based on the investigation of the PL temperature dependence allowed to demonstrate a much lower defect trap states in nanorods. Moreover, a much higher stability of the nanorods with respect to the nanocubes was also demonstrated during heating and during immersion in water. Finally, outstanding ASE properties were demonstrated under 1 ns pumping at 355 nm, with an ASE threshold as low as 7.5 μJcm^{-2} (see Figure 3b,c) , comparable with the values typically found for femtosecond pumping. For the sake of comparison we observe that the ASE threshold of $CsPbBr_3$ nanocubes under nanosecond pumping is typically in the range between 450 μJcm^{-2} and a few mJcm^{-2} [5,30].

The main ASE (wavelength and threshold) and pump laser properties (wavelength and time length) of all the discussed materials are summarized in Table 1.

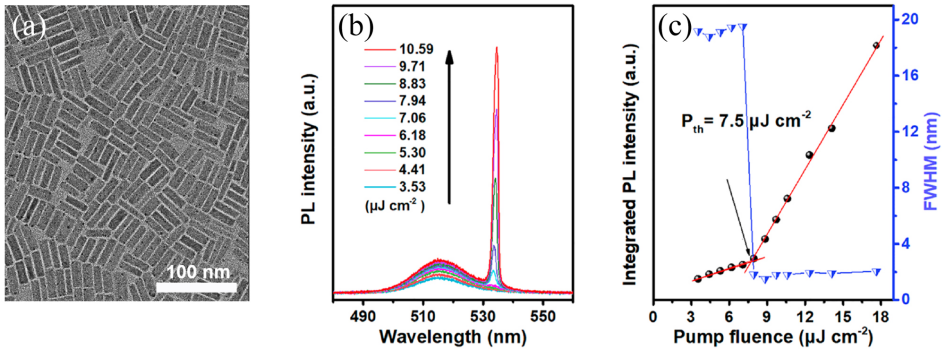

Figure 3. (**a**): TEM image of $CsPbBr_3$ nanorods. (**b**): excitation density dependence of the PL spectra. (**c**): Excitation density dependence of PL spectrum intensity and linewidth. Adapted with permission from [38]. American Chemical Society, 2019.

Table 1. ASE properties of the perovskites described in this review. The data are grouped according to the active material and in order of increasing pump pulse time length. For papers discussing multiple samples with the same material the reported data are relative to the sample with the minimum threshold.

Active Material	Threshold	Peak wav. (nm)	Pump Pulse Length	Pump wav. (nm)	Ref.
$MAPbI_3$	26.5 μJcm^{-2}	793	120 fs	520	[15]
$MAPbI_3$	12 μJcm^{-2}	788	150 fs	600	[4]
$MAPbI_3$	7.6 μJcm^{-2}	780	5 ns	532	[12]
$MAPbI_3$	54.1 μJcm^{-2}	≈780	5 ns	500	[16]
$MAPbI_3$	47 μJcm^{-2}	793	7ns	520	[15]
$MAPbI_3$-PMMA	16.9 μJcm^{-2}	793	120 fs	520	[15]
$MAPbI_3$-PMMA	600 μJcm^{-2}	≈780	1 ns	533	[19]
$MAPbI_3$-PMMA	31 μJcm^{-2}	793	7 ns	520	[15]
$MAPbI_{3-x}Cl_x$	50 μJcm^{-2}	≈800	0.88 ns	337	[20]
$MAPbBr_3$	303 μJcm^{-2}	549	1 ns	355	[13]
$MAPbBr_3$	45 μJcm^{-2}	≈552	1 ns	355	[18]
$MAPbBr_3$	35 μJcm^{-2}	550	5 ns	444	[17]
$MAPbBr_3$-PMMA	140 μJcm^{-2}	549	1 ns	355	[13]
$FAPbI_3$	3.0 μJcm^{-2}	812	150 fs	400	[21]
$FAPbI_3$	19.5 μJcm^{-2}	812	5 ns	532	[21]
$CsPbBr_3$	3.3 μJcm^{-2}	≈545	150 fs	400	[23]
$CsPbBr_3$	12.5 μJcm^{-2}	541	300 ps	355	[24]
$CsPbBr_3$	26 μJcm^{-2} (10 K)	534	3 ns	337	[22]
$CsPbBr_3$	64.9 μJcm^{-2}	≈545	5.5 ns	355	[23]
$CsPbCl_3$ NCs	10.9 μJcm^{-2}	460	100 fs	400	[5]
$CsPbCl_{1.4}Br_{1.6}$ NCs	≈48 μJcm^{-2}	475	100 fs	400	[29]
$CsPbBr_3$ (OA)NCs	193.5 μJcm^{-2}	538	50 fs	400	[36]
$CsPbBr_3$ (DA) NCs	89.76 μJcm^{-2}	538	50 fs	400	[36]
$CsPbBr_3$ NCs	2 μJcm^{-2}	535	100 fs	400	[35]
$CsPbBr_3$ NCs	5.3 μJcm^{-2}	530	100 fs	400	[5]
$CsPbBr_3$ NCs	≈38 μJcm^{-2}	502	100 fs	400	[29]
$CsPbBr_3$ NCs	450 μJcm^{-2}	530	10 ns	355	[5]
$CsPbBr_3$ nanorod	7.5 μJcm^{-2}	534	1 ns	355	[38]
$CsPbBr_{0.8}I_{2.2}$ NCs	≈55 μJcm^{-2}	620	100 fs	400	[29]
$CsPbI_3$ NCs	22 μJcm^{-2}	630	100 fs	400	[5]
$MAPbBr_3$ NCs	3 μJcm^{-2}	545	100 fs	400	[31]
$MAPbBr_3$ NCs	14 μJcm^{-2}	548	150 fs	400	[37]
$FAPbI_3$ NCs	7.5 μJcm^{-2}	808	100 fs	400	[33]
$FAPbI_3$ NCs	140 μJcm^{-2}	808	4 ns	532	[34]
$FA_{0.1}Cs_{0.9}PbI_3$ NCs	28 μJcm^{-2}	720	100 fs	400	[33]

3. Optically Pumped Lasers

The capability of a material to show ASE is a direct consequence of the presence of optical gain, and thus naturally opens the way to its employment as active material of a LASER. Despite the acronym meaning (Light Amplification by Stimulated Emission of Radiation) in order to realize a LASER it is necessary to combine a light amplifying material with a suitable feedback mechanism, allowing the light to efficiently propagate along round trips in the active material only for specific wavelengths, being amplified in any round trip. This result can be obtained with a wide variety of resonators, allowing to reach different levels of control on the lasing efficiency, the laser light directionality, the chromatic composition (single wavelength of multiple wavelength) and the coherence. Last but not least, the different kinds of resonators have different realization complexities. In the following section, we will discuss the main results on several types of perovskite lasers, in order of increasing realization complexity. We will start from random lasers, in which the lasing feedback comes from constructive interference of light scattered during its propagation in the active material, and we will then move to whispering gallery mode lasers (WGM), typically exploiting light propagation in cavities with size of tens of microns. Finally, we will describe the development and the current state of the art of Distributed Feedback Lasers (DFB) and the Vertical Cavity Surface Emitting Lasers (VSELs), both requiring nanofabrication and/or deposition techniques with a control on the tens of nanometers scale.

3.1. Random Lasers

Random lasers are the simplest systems in which it is possible to observe narrow and coherent emission from a material showing optical gain. The lasing feedback is provided by constructive interference of the light partially scattered during its propagation in the active material. As light scattering can be obtained simply from morphological irregularities of the active film, random lasing is often observed also in experiments aiming to characterize the ASE and gain properties of thin films, whose surface morphology often present defects acting as scattering centers. The first experiment on perovskites random lasers [39] was published only a few months after the demonstration of ASE from $MAPbX_3$ thin films [4] and basically exploited the tendency of perovskites materials to form films with morphological defects. In particular, the authors deposited a $MAPbI_3$ film, by spin coating a 20% in weight dimethylformamide (DMF) precursor solution containing CH_3NH_3I and PbI_2 mixed in a 1:1 molar ratio. They observed the spontaneous formation of a network of planar elongated microcrystals, with a typical length of about 50 μm and a typical thickness in the range 300–500 nm (see Figure 4e).

The emission spectra of the sample, under pumping with a 0.8 ns pulsed UV laser at 335 nm, showed only the broad unstructured band-edge photoluminescence typical of the $MAPbI_3$ at low pump fluence, with a peak wavelength at 765 nm . When the excitation density increased above 200 μJcm^{-2} sharp peaks appeared in the spectra (see Figure 4a) and become progressively more evident as the excitation density was further increased. The appearance of the narrow peaks also leaded to a variation in the slope of the PL intensity increase with the excitation density (see Figure 4b), which is the typical signature of lasing threshold. The local emission properties of the sample were investigated by micro-PL measurements showing evidence of (see Figure 4c,d) the appearance of bright spots in the PL maps at excitation densities above the random lasing threshold, in positions corresponding to the junctions within the different microcrystals. This result suggested that light mainly propagated along the individual crystals, and it was then scattered at the crystals junctions thus forming random closed loops determining the lasing wavelengths.

A couple of years later a further experiment was performed on $MAPbI_3$ films deposited by a two step spin coating of a PbI_2 solution in DMF, followed by a methylammonium iodide (MAI, CH_3NH_3I) in 2-propanol (IPA) [40]. This deposition procedure allowed to obtain a film with a thickness of about 450 nm, with a full surface coverage and a grainy structure, with an average grain size of about 200 nm (see Figure 5a). The excitation density dependence of the PL spectra, under 1 ns UV pumping at 335 nm, showed the appearance of random lasing peaks, with a threshold reduced to 102 μJcm^{-2} (see Figure 5b), whose number and intensity increased with the excitation density. This result was

ascribed to random lasing considering that the formation of standard resonant cavities within the individual grains can be excluded both due to the irregular grains shape and size and to the irregular evolution of the number and the wavelength of the lasing modes as the excitation density increased.

The proposed lasing mechanism is schematically depicted in Figure 5c, considering the randomly arranged $MAPbI_3$ grains both as the gain media and the multiple scattering sources. The emitted light undergoes multiple scattering at the grain boundaries eventually returning to a path from which they were scattered before, thus forming closed-loop cavities and providing lasing oscillation at the resonant frequency of the corresponding feedback loop when the optical gain exceeds the losses.

These evidence of morphological defects inducing random lasing stimulated further research aiming to control the lasing properties of the samples by acting on the film structure and morphology.

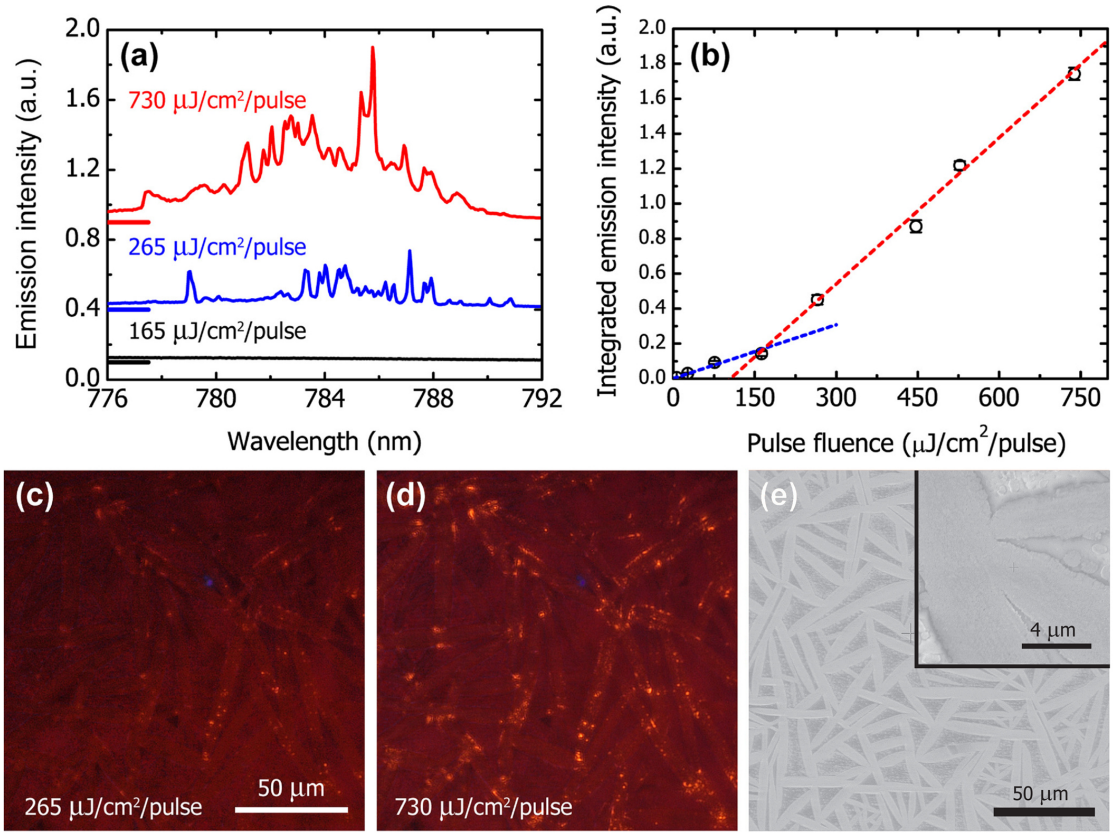

Figure 4. (**a**) Emission spectra collected below (black), near (blue), and above lasing threshold (red). The spectra were offset vertically for clarity; horizontal line-segments at the left of each spectrum indicate their corresponding zero-levels. (**b**) Integrated emission intensity as a function of excitation pulse fluence, showing evidence of the presence of a slope variation due to the random lasing threshold. (**c**,**d**) Micro-PL images showing the spatial distribution of emission at the two highest pump intensities in (**a**). Bright spots observed in (**d**) above threshold correspond to high scattering locations where laser light is efficiently out-coupled from the perovskite network, as also evident by the comparison with the SEM image (**e**). Adapted with the permission from [39]. AIP Publishing, 2014.

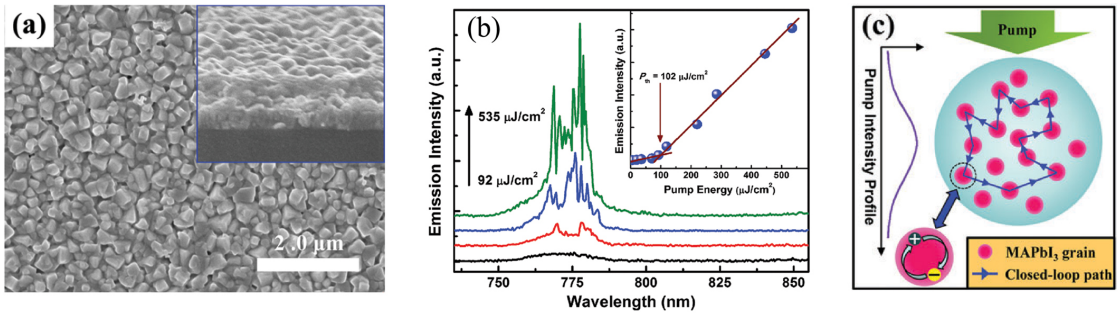

Figure 5. (**a**) SEM image of the $CH_3NH_3PbI_3$ film showing evidence of the presence of cuboids with a typical size of about 200 nm. The inset shows the sample cross section. (**b**) Excitation density dependence of the PL spectra of the film, showing evidence of the progressive appearance of random lasing peaks as the excitation density increases. Inset: excitation density dependence of the PL intensity, showing the random lasing threshold. (**c**) Pictorial view of the formation of a closed-loop laser cavity via random scattering provided by the polycrystalline grain boundary. Adapted with permission from [40]. Royal Chemical Society, 2016.

A possible approach in this direction is based on the variation of the sample preparation conditions, in order to modify its morphology. For example, Cao et al. compared the emission properties of $MAPbI_3$ films obtained by a two step spin coating process, using four different concentrations of the PbI_2 DMF solution (namely 10%, 20%, 30% and 40% in weight) [41]. The films morphology showed an inhomogeneous substrate coverage, with a rugged surface and randomly distributed grains when the 10% PbI_2 solution was used and a progressive morphology improvement for higher concentrations. In particular the sample from the 10% PbI_2 solution was characterized by an air-void occupation area of about 50%, progressively decreasing down to about 2% for the film deposited from the 40% PbI_2 solution. The emission spectra of the films were investigated at a temperature of 77 K, showing a clear ASE band as the excitation density increased, with a threshold depending on the film, and an evident modulation due to random lasing in the sample deposited from the 30% PbI_2 solution. The ASE and lasing differences between the samples were ascribed to the variation of the morphology, changing the balance between optical gain and grain boundaries scattering.

More recently morphological differences were observed by depositing $MAPbI_3$ films by spin coating of a PbI_2 DMF solution, followed by dipping for various times in a solution of MAI in IPA [42]. The dipping time also affected the film emission properties, showing only spontaneous emission, ASE or random lasing depending on the preparation conditions.

Enhanced random lasing was also claimed in $CsPbBr_3$ thin films thanks to the addition of ZnO nanoparticles to the perovskite precursor solution [43]. In this experiment, no lasing like peaks were present in the PL spectra at high excitation density, providing evidence of the lack of coherent scattering in the films. The smaller ASE threshold in the ZnO containing film was ascribed to smaller crystalline grains of the film and lower density of air voids on the film surface, related to the scattering efficiency of the film.

A second possibility to introduce, and control, scattering in the samples is the deposition of the active film on a structured substrate. A first demonstration of this approach was obtained by depositing $MAPbBr_3$ nanocrystals on a substrate corrugated by strain release wrinkles [44]. The sample was realized by unidirectionally stretching a polydimethylsiloxane (PDMS) film up to 100% of its original length and by depositing on it a graphene oxide (GO) layer and a NCs layer. The difference in elastic constant between PDMS, GO and NCs leads to an almost unidirectional corrugation of the surface when the strain is released. The correlation between the wrinkles formation and the random lasing was demonstrated by measuring the PL spectra, at high pumping density, progressively removing the strain and observing that only spontaneous emission was present when the PDMS-GO substrate was fully strained (and thus planar), while random lasing peaks appeared when the residual strain decreased below 60%. The possibility to control the wrinkle size and geometry by engineering the

strain conditions of the substrate opens the way to the realization of random lasers with optimized emission properties. While this result is still not present in perovskites random lasers it was recently demonstrated that the control of the wrinkles height, shape and size allows to realize organic active layers showing random lasing, ASE or even no light amplification [45].

A further elegant experiment on the perovskite random lasing engineering was recently performed by Roy et al. [46] that deposited $MAPbBr_3$ NCs on a network of graphene-sheathed SiC nanowalls (EGNWs) (see Figure 6a). The sample PL spectra clearly showed coherent random lasing peaks with a very low threshold of 10 $nJcm^{-2}$ (see Figure 6c), under 55 ps pumping at 374 nm, ascribed to the extremely high photon trapping within the graphene network. As further step the authors improved the scattering properties of the EGNWs by coating them with 40 nm of Ag nanoparticles and then with 100 nm of SiO_2. This coating process left basically unaltered the EGNWs morphology (see Figure 6b) but strongly improved the scattering cross section, due to the plasmonic field enhancement induced by the Ag nanoparticles. The random lasing properties of the EGNW-Ag-NCs samples were similar to the EGNW-NCs one, due to the interplay between improved scattering and non radiative NCs emission quenching, both due to the Ag plasmons. On the contrary a remarkable improvement of the emission properties showed both by a PL intensity increase and by a random lasing threshold decrease of one order of magnitude was observed in the EGNW-Ag-SiO_2-NCs samples due to suppression of the PL quenching at the Ag/PNCs interface induced by the incorporation of the SiO_2 spacer layer.

Despite the attempts to control their emission properties the applicative perspectives of random lasers are to date still limited by the lack of reproducibility of mode wavelength and threshold from sample to sample, and by the poor directionality of the emission, which makes unrealistic any claim of their use in applications requiring the emission features of standard lasers (monochromaticity, directionality and spatial and temporal coherence). Anyway the multimode emission and the low spatial coherence propose random lasers as bright and cheap sources for applications in which coherence can produce artifacts, like the speckle patterns formation in illumination. A nice evidence of the perovskite random lasers potentialities as speckle free lighting sources was very recently obtained in $MAPbBr_3$ thin films deposited by spin coating and showing a morphology dominated by the aggregation of irregular perovskite islands with an in-plane size in the range 20–80 µm [47]. Coherent random lasing with a threshold of about 91 μJcm^{-2} was observed, under 100 fs pumping at 400 nm, ascribing the feedback to scattering at the islands edges. To improve the random lasing directionality the active layers were also put in a Distributed Bragg Reflector (DBR) cavity showing multimode emission due to the thickness irregularities of the perovskite layer, thus combining directionality and low spatial coherence. The speckle contrast in a test imaging application was then measured, providing evidence of a contrast 7.6 times lower than the one of a standard laser diode and 2.7 times larger than white light, but with much brighter emission.

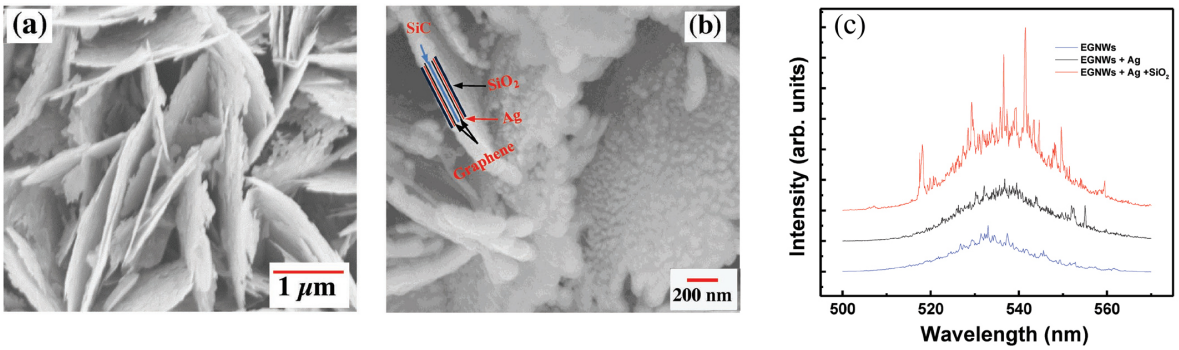

Figure 6. (**a**) Top FE-SEM image showing the morphology of the epitaxial graphene nanowalls (EGNWs) grown on Si (111) using MPECVD. (**b**) Cross-sectional view of one nanowall after coating with the Ag/SiO_2 layers. The lines are guides to the eye and do not resemble in exact scale the constituent layers. (**c**) Emission spectra of EGNWs/PNC, EGNWs/Ag/PNC, and EGNWs/Ag/SiO2/PNC at a constant pump density of 14.19 $nJcm^{-2}$. Adapted with permission from [46]. John Wiley and Sons, 2018.

3.2. Whispering Gallery Mode (WGM) Lasers

The name whispering gallery was originally introduced for architectonic buildings (typically domes) in which weak sounds emitted close to the walls can be easily heard even at large distances. This process is basically related to sound reflections and refocusing from the curved walls, which allows efficient sound propagation. The optical analogous of these systems are dielectric cavities with regular shape, like spheres, disks and rings containing a luminescent material. Under optical excitation the PL emitted by the active material propagates within the structure, experiencing total internal reflections at the cavity edges. For proper wavelengths the emitted waves make an integer number of oscillation in any closed loop, thus forming standing waves at discrete wavelengths. If the active material is pumped above the optical gain threshold this system emits multimode laser light. The technological reasons of interests of WGM lasers are related to the typical cavity size required to obtain a few modes in the visible range, that is of the order of tens of microns, which can be easily realized by standard photolithography. Moreover, many active materials, including perovskites, spontaneously form micrometric crystals or domains in the films with regular shape, thus allowing the realization of self assembled micrometric lasers. In this section we review the main results recently published on perovskites WGM lasers, starting from the self assembled ones and concluding with the lithographically realized cavities.

The simplest perovskites systems showing lasing in WGM resonators were obtained in $MaPbI_{3-a}X_a$ (X = I, Br, Cl) nanoplatelets, spontaneously formed during vapor transport chemical vapor deposition (CVD) on a mica substrate [48]. The nanoplatelets show a regular geometry, with triangular or hexagonal shape with an edge length in the range 5–50 μm, a thickness in the range 20–300 nm and an extremely low surface roughness of about 5 nm (see Figure 7a). Clear diffraction patterns of the pump laser were observed in single platelets (see Figure 7a), indicating good optical confinement in the nanoplatelet WGM cavities. The excitation density dependence of the PL spectra of individual nanoplatelet, under 50 fs pumping at 400 nm, showed only spontaneous emission at low excitation density, and the appearance of several sharp peaks centered around 780 nm, with a linewidth of about 1.2 nm and a constant distance between consecutive peaks of about 2.5 nm (see Figure 7b). The presence of equally spaced modes is the typical signature of multimodes resonant cavities. Further evidence of lasing were obtained by investigating the excitation density dependence of the emission intensity, showing a clear slope variation at the lasing threshold of about 37 μJcm^{-2} (see Figure 7b left inset), and of the emission lifetime, showing a long average spontaneous emission lifetime of about 2.6 ns below the threshold and a much lower resolution-limited lifetime of about 80 ps above the threshold, due to the fast excited state depletion induced by lasing (see Figure 7b right inset).

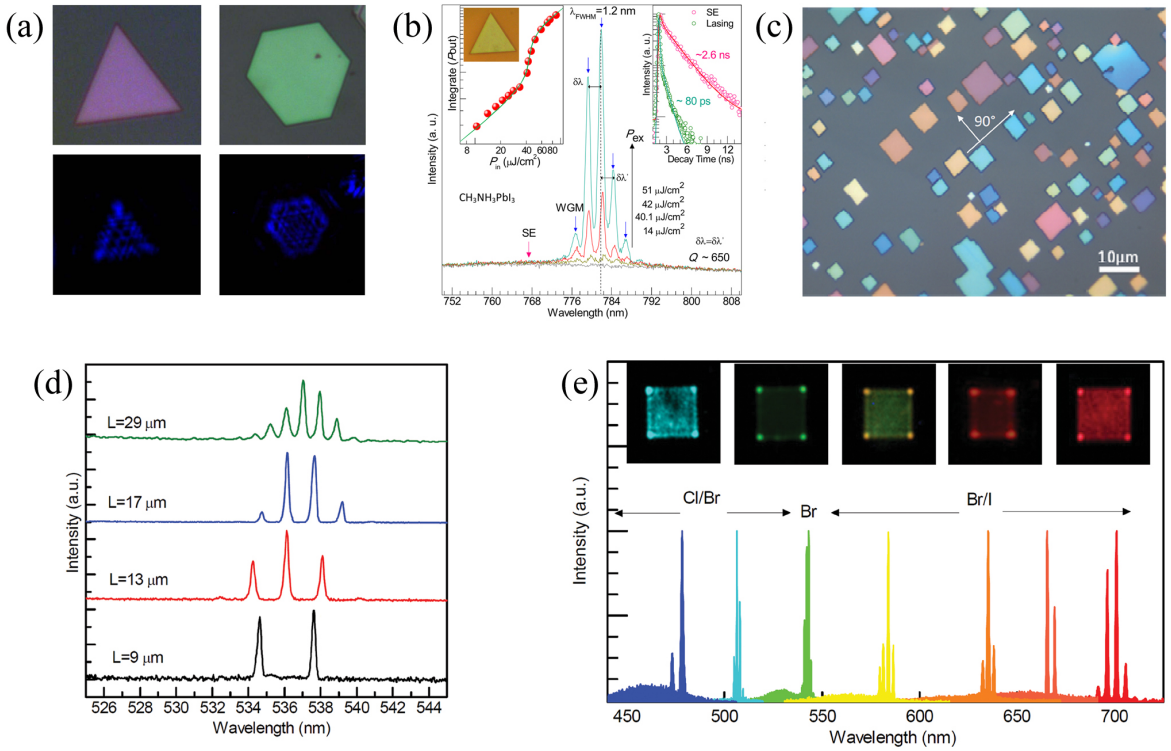

Figure 7. (**a**) Far-field optical image of two typical $MAPbI_3$ nanoplatelets under the illumination of white light (upper panel) and pump laser (bottom panel) providing evidence of clear diffraction patterns inside the WGM cavity. (**b**) Excitation density dependence of the PL spectra of a typical $MAPbI_3$ triangular nanoplatelet (optical image inset; thickness, 150 nm; edge length, 32μm). Left inset: integrated output emission (P_{out}) over the whole spectra range as a function of pumping fluence (P_{in}) using log-log scale, providing evidence of the lasing threshold. Right inset: PL relaxation dynamics below (pink, SE) and above (dark green, lasing) the threshold. (**a**,**b**) adapted with permission from [48]. American Chemical Society, 2014. (**c**) Optical image of $CsPbBr_3$ nanoplatelets showing square or rectangular shapes and rich colors. (**d**) Multimode lasing spectra of four nanoplatelets with different edge length from 9 to 29 μm. (**e**) Multicolor WGM microlasers based on inorganic perovskites with different composition. (**c**–**e**) adapted with permission from [49]. John Wiley and Sons, 2016.

A couple of years later, the same group realized, with the same technique, fully inorganic $CsPbX_3$ (X = I, Br, Cl) nanoplatelets [49], showing a well-defined square and rectangular shapes (see Figure 7c), ascribed to the intrinsic cubic crystalline phase of the perovskite. The optical images of the nanoplatelets showed rich colors, due to interference effect between the light reflected from the top and from the bottom surfaces, and to different nanoplatelets thickness in the 50–300 nm range. Also In this case, as the excitation density increased the emission spectra revealed the appearance of multiple, equidistant, narrow peaks, with much lower linewidth (down to 0.15 nm), with a threshold decreased to 2.2 μJcm^{-2}, under 50 fs pumping at 400 nm.

As further characterization, the authors also investigated the lasing spectra dependence on the edge length, observing a progressive reduction of the number of lasing modes and an increase of their spacing as the edge length was progressively decreased from 29 μm to 9 μm (see Figure 7d). Finally full color tuning was demonstrated by acting on the chemical structure in ternary and quaternary compounds, all showing lasing threshold below 10 μJcm^{-2} (see Figure 7e). Very similar results were also obtained by depositing square $CsPbX_3$ (X = I, Br, Cl) nanoplatelets by CVD on Si/SiO_2 and sapphire [50].

An alternative deposition approach was proposed by Sasaki et al. that demonstrated WGM lasing from $MAPbBr_3$ microstructures realized from solution [51,52], reducing the solvent evaporation rate

by covering the solution with a second substrate. Even if simple, this technique allowed the realization of microcrystals with a larger variety of shapes, including disks, squares and rectangles.

Tridimensional $MAPbBr_3$ microcrystals were instead obtained by a single step deposition process from solution, consisting of the deposition of a precursor solution in DMF and drying in a sealer beaker containing dichloromethane as antisolvent [53]. The diffusion of dichloromethane in the solution induced the nucleation and the subsequent growth of square 3D microcrystals with very smooth outer surface and sharp edges (see Figure 8a). Single mode lasing with a threshold as low as 3.6 μJcm^{-2}, under 120 fs pumping at 400 nm, was demonstrated in a square microcrystal with a edge length of 2.0 μm, while at higher edge lengths multimode lasing was observed. The same technique was also exploited to realize fully inorganic $CsPbBr_3$ parallelepiped microrods, with length in the 2–8 μm range and height in the range 1–5 μm, thus big enough to allow WGM formation (see Figure 8b) [54], and even branched microrods (see Figure 8c) [55].

A detailed description of the growth process leading to the spontaneous formation of parallelepiped microcrystal was reported by Zhou et al. that deposited cubic $CsPbBr_3$ microcubes by dual source CVD [56]. By investigating the shape of the microcrystals formed on substrates in different positions in the furnace tubes, and thus grown at different temperatures, the authors observed (see Figure 8d) that the microparticles formed at lower temperature have a poor crystallinity and a spherical shape, in order to minimize the internal energy. At higher temperatures a crystallinity increase was observed, resulting in a progressive shape transition toward cubes with well-defined facets and edges. A short growth time leads to the formation of cubic microcrystals, while long times result in appreciable edges length differences due to growth rate dependence on the facets orientation, thus resulting in parallelepiped microcrystals. Single mode lasing was again observed in small microcubes both under 80 femtoseconds pumping at 470 nm, with a threshold of 16.9 μJcm^{-2} and a remarkably low linewidth of 0.064 nm, and under 1.1 nanosecond pumping at 355 nm, with a higher threshold of 214 μJcm^{-2}.

Another fascinating demonstration of the perovskite capability to spontaneously form complex structures was recently obtained by Li et al. that realized [57] $MAPbBr_3$ microcubes by a solvatothermal process at a temperature of 120 °C, observing the initial formation of cubic microcrystals with an edge length increasing to about 10 μm with the reaction time, followed by the formation of a step on the (001) surfaces and, as the reaction time further increased, of a multistep structure inside the microcubes (see Figure 8e).

All these approaches show that perovskites have the capability to form bidimensional or tridimensional microcrystals with well-defined polygonal or polyedron shape if the growth process is adequately controlled, providing easy microcavity formation processes that allow to test the lasing properties of a given active material. However these spontaneously formed microlasers are not suitable for real devices applications as the lasing properties in terms of threshold and lasing wavelength are different between individual microcrystals and basically impossible to control and predict *a priori*.

For this reason several groups worked to realize WGM microresonators with reproducible spectra and thresholds.

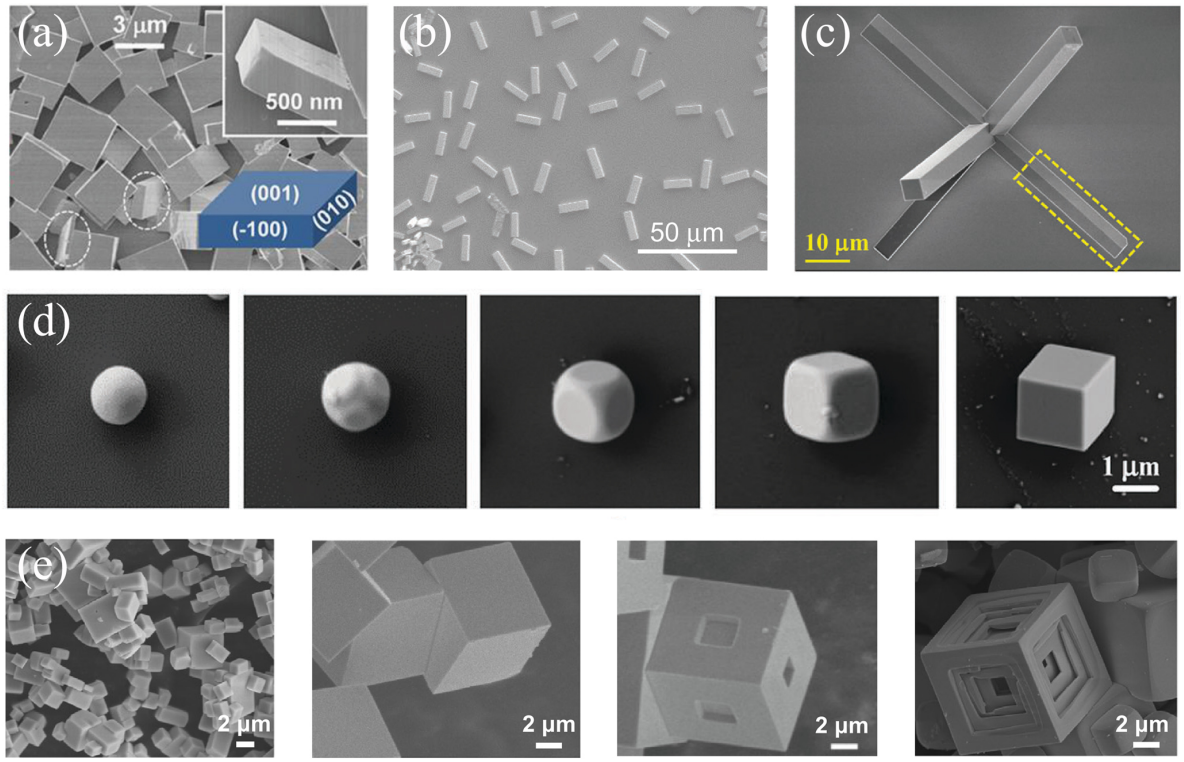

Figure 8. SEM images of (**a**) parallelepiped microcrystals of bromide perovskite $MAPbBr_3$ at low magnification and high magnification (top inset). The circled regions indicate the thickness of square MDs. The right bottom inset shows a cartoon of a square MD. Adapted with permission from [53]. John Wiley and Sons, 2015. (**b**) $CsPbBr_3$ microrod. Adapted with permission from [54]. John Wiley and Sons, 2015. (**c**) $MAPbBr_3$ branched microrod. Adapted with permission from [55]. Royal Society of Chemistry, 2017. (**d**) $CsPbBr_3$ microcubes at different growth stages with increasing temperature. Adapted with permission from [56]. Royal Society of Chemistry, 2018. (**e**) $MAPbBr_3$ cuboids at different reaction times. Adapted with permission from [57]. Elsevier, 2019.

A first possibility in this direction is the micropatterning of the substrate, in order to guide the spontaneous formation of identical microcavities. A nice demonstration of this approach was reported by Liu et al. [58] that realized hexagonal micropatelets with an edge length of about 15 μm of $MAPbI_3$ by physical vapor deposition on a Si substrate covered by a single layer boron nitride (BN), prepatterned in hexagons by photolitography. The BN hexagons act as nucleation centers for the perovskites, allowing the growth of $MAPbI_3$ crystals replicating the BN geometry. Multimode lasing was observed, under 50 fs pumping at 400 nm, with a threshold down to 9 μJcm^{-2} and single mode lasing was demonstrated for edge length shortened to about 2 μm. The authors also demonstrated the possibility to obtain single mode lasing in larger microcrystals by acting on the crystal geometrical symmetry rather than on its size, obtaining a single mode in asymmetric hexagonal crystal with an edge lengths between 5 and 10 μm and with a threshold about 3 times smaller than the 2 μm regular hexagon (see Figure 9a–d).

Another fascinating approach to obtain arrays of microcrystals with similar shape and size is the template confined growth from solution. In this case, a precursor solution is deposited on a substrate and covered by a PDMS mold with patterned voids. The PDMS is then pressed on the substrate, leaving the solution only in the mold voids. The slow solvent evaporation in a geometrically confined region leads to perovskite crystallization and to the formation of microcrystals of the same shape and size. For example He et al. [59] realized an array of $CsPbCl_3$ square microplates, showing a rather uniform edge length of 2.5 ± 0.3 μm, and multimode lasing around 427 nm. The comparison of the lasing spectra of nine different platelets anyway showed differences in the number and in the

wavelengths of the lasing modes and in the threshold, ascribed to the slight edge length differences between the individual platelets. The authors also developed a vapor-phase halide exchange method in order to integrate on the same substrate microlasers operating at different colors, based on the protection of part of the platelets with scotch tape followed by exposure to HBr vapors. They interestingly observed that the uncovered platelets converted from deep blue $CsPbCl_3$ to green $CsPbBr_3$ while the platelet far from the tape edge remained unaltered. Partial composition conversion took instead place in the platelets close to the tape edge, thus allowing a color tuning including blue and cyan (see Figure 9e).

A remarkable improvement of the lasing reproducibility was demonstrated by the same group that succeeded in the realization [60], with the same technique, of microrings of 2D Ruddlesden-Popper $(BA)_2(MA)_{n-1}Pb_nBr_{3n-1}$ (see Figure 9f–h) showing very similar spectra between different lasers with maximum relative threshold variations of about 10%.

Finally, almost aligned $CsPbBr_3$ microwire WGM lasers were recently realized by a PDMS template-confined antisolvent crystallization method, obtaining a good control of wire length, width and position [61]. Strain induced dynamic modulation of the lasing modes was also demonstrated and ascribed to piezoeletric polarization effects on the $CsPbBr_3$ gain region and refractive index.

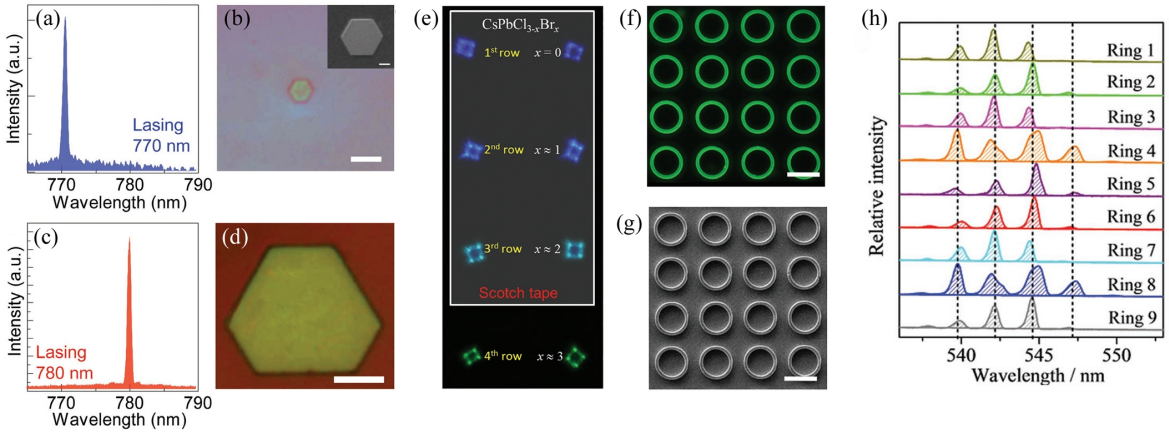

Figure 9. (**a**) Single mode lasing spectrum from a small $MAPbI_3$ microhexagon with edge length of 2 μm, shown in (**b**) (optical microscope image, size bar 5 μm and SEM image in the inset, size bar 1 μm). (**c**) Single mode lasing spectrum from a large $MAPbI_3$ asymmetric microhexagon, shown in (**d**) (optical microscope image, size bar 5 μm). (**a**–**d**) Adapted with permission from [58]. John Wiley and Sons, 2016. (**e**): Optical microscope image of $CsPbCl_{3-x}Br_x$ above the lasing threshold providing evidence of lasing color tuning by controlled halide exchange. Adapted with permission from [59]. John Wiley and Sons, 2017. (**f**–**g**) Low magnification microPL and SEM images of 2D perovskites microrings. (**h**) Lasing spectrum of 9 different microrings, providing evidence of the reproducibility. (**f**–**h**) Adapted with permission from [60]. John Wiley and Sons, 2018.

Another strategy to realize resonant cavity with controlled and reproducible size and shape, still preserving the easy realization, is given by the perovskite growth on dielectric resonators, like microspheres [62,63] or microcapillaries [64]. The first results with this approach were obtained by Sutherland et al. [62] that developed a growth process allowing the conformal coating of a SiO_2 microsphere, with a diameter of 52 μm, with a $MAPbI_3$ film with excellent thickness uniformity (see Figure 10a). The growth was obtained starting with atomic layer deposition of PbS on the microsphere, followed by its conversion to PbI_2 by exposure to I_2 vapors and concluding with the conversion to $MAPbI_3$ through treatment with MAI. The samples showed WGM lasing under 2 ns pumping at 355 nm and at a temperature of 80 K with a threshold of about 75 μJcm^{-2}. Room temperature single mode lasing was more recently demonstrated in $CsPbX_3$ microspheres with a diameter of about 1.0 μm realized by standard CVD (see Figure 10b).

An alternative approach to realize WGM perovskite lasers is based on the crystals growth within a SiO_2 microcapillary, acting on the inner diameter in order to control the cavity size. A good demonstrator of this approach is provided by $MAPbBr_3$ lasers realized by filling the capillary with the perovskite precursors and controlling the solvent evaporation rate in an air oven. In this way a polycrystalline material can be grown within the capillary (see Figure 10c,d) and lasing features tunable by simply changing the capillary diameter can be obtained.

A notably seldom reported approach to realize WGM resonators with controlled geometry is the direct lithography on the perovskite active film, as these techniques most of the time need the use of solvents or of resists that irreversibly damage the perovskite film. An important recent breakthrough is the realization of $MAPbBr_3$ microdisks by top-down e-beam lithography followed by ICP etching [65]. The whole process preserved the perosvkite film integrity and allowed the realization of lasers showing low threshold, narrow lines and, more importantly, excellent spectral reproducibility between different devices on the same substrate (see Figure 10e). The authors also demonstrated the realization of unidirectional emission from asymmetric elliptical resonators.

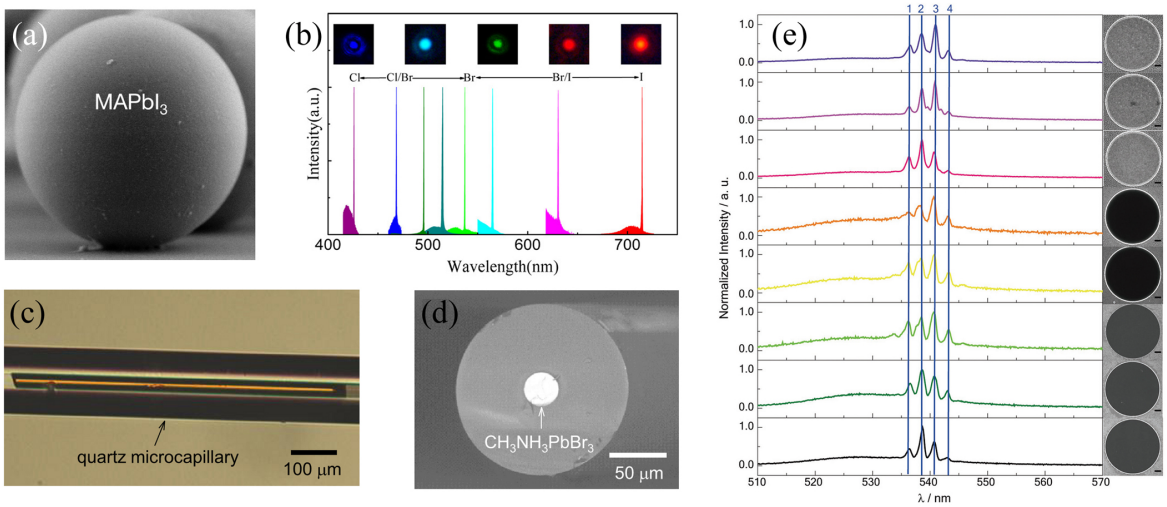

Figure 10. (**a**) SiO_2 microsphere coated with a $MAPbI_3$ thin film. Adapted with permission from [62]. American Chemical Society, 2014. (**b**) Single mode tunable lasing in $CsPbX_3$ spheres with different chemical composition. Adapted with permission from [63]. American Chemical Society, 2017. (**c**) Optical micrograph of $MAPbBr_3$ crystals grown in a SiO_2 microcapillary with internal diameter of 25 μm. (**d**) Cross sectional SEM image of the same sample. (**c**,**d**) adapted with permission from [64]. AIP publishing, 2018. (**e**) Lasing spectra of 8 different $MAPbBr_3$ microdisks realized by top-down lithography providing evidence of the excellent spectral reproducibility. Adapted with permission from [65]. John Wiley and Sons, 2017.

3.3. Distributed Feedback (DFB) Lasers

DFB lasers are basically made by an active waveguide, in which a periodic modulation of the refractive index along the light propagation direction allows constructive interference between the partially reflected components at the wavelengths satisfying the Bragg condition $2n_{eff}\Lambda = m\lambda$ (where n_{eff} is the effective refractive index of the waveguide, Λ the grating period, m the interference order and λ the light wavelength). The feedback for lasing comes from partial reflection at any refractive index variation, and it is thus distributed along the film. Moreover, the light propagation along the films results in large amplification, thus allowing to combine single mode operation (for small enough grating period) with efficient amplification along the active film. The refractive index periodic modulation is typically obtained by realizing periodic unidimensional gratings either on the substrate/film or on the film/air interfaces (see Figure 11a). This allows the realization of DFB lasers by simple deposition of the active film on a properly patterned substrate or by imprinting the

top surface with a patterned stamp, after the film deposition, by soft lithography techniques, thus avoiding any wet lithography that can damage the perovskites layer.

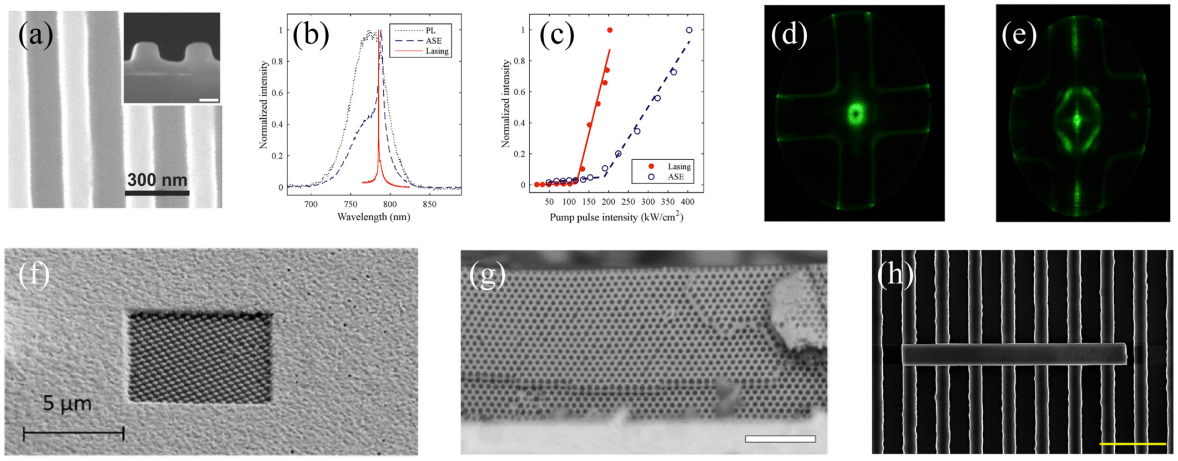

Figure 11. (**a**) SEM images of the DFB grating imprinted into a $MAPbBr_3$ layer with a periodicity of 300 nm (inset: high resolution cross-section, scale bar is 100 nm). Adapted with permission from [66]. John Wiley and Sons, 2018. (**b**) PL, ASE, and DFB lasing spectra of $MAPbI_3$. (**c**) Emission intensities at the peak wavelengths as a function of the pump pulse intensity of the same $MAPbI_3$ sample in a position without and with underlying grating, leading to ASE (blue) and lasing (red) at thresholds of 190 μJcm^{-2} ($\pm$38 μJcm^{-2}) and 120 μJcm^{-2} ($\pm$24 μJcm^{-2}), respectively. (**b**,**c**) adapted with permission from [67]. AIP publishing, 2016. (**d**,**e**) Photograph of the output beam of a $MAPbBr_3$ DFB laser projected on a screen, (**d**) shows the TM mode from a 300 nm grating, while (**e**) shows the TE mode from a 290 nm grating. (**d**,**e**) adapted with permission from [18]. Springer Nature Publishing, 2017. (**f**) SEM image at a 52° inclination with respect to the normal of a $MAPbI_3$ film on top of a 2D grating with a portion of the perovskite removed by focused ion beam to evidence the underlying pattern. Adapted with permission from [68]. OSA Publishing, 2016. (**g**) Cross-sectional SEM of a $MAPbBr_3$ inverse opal (scale bar 2 µm). Adapted with permission from [69]. American Chemical Society, 2017. (**h**) Top-view SEM image of a $MAPbBr_3$ microwire on silicon grating with a periodicity of 5 µm (scale bar 10 µm). Adapted with permission from [70]. American Chemical Society, 2016.

The first demonstration of single mode DFB optically pumped perovskite lasers was obtained by Brenner et al. [67] by depositing a $MAPbI_3$ thin film from solution on the polymeric replica of a silicon master pattern, obtained by nano imprint lithography (NIL). The excitation density dependence of the emission spectra, under 1 ns pumping at 532 nm, allowed to observe the appearance of a very narrow peak at 786.5 nm, with a resolution limited linewidth of 0.2 nm, above a threshold excitation density of 120 μJcm^{-2} (see Figure 11b,c). To unambiguously demonstrate that these features were due to lasing the authors also compared the threshold and the linewidth with the ASE ones, measured on the same film in a planar region of the substrate. They observed that the ASE linewidth and threshold were both higher than the values found in the region of the substrate pattern. Moreover the polarization of the emission was measured, demonstrating that the ASE is not polarized, while the laser peak has a clear linear polarization.

After this first breakthrough the same group also realized the first flexible perovskite DFB laser by ink-jet printing deposition of $MAPbI_3$ [71]. In this case, a pattern realized on silica was replicated by PDMS, then the PDMS stamp was used to transfer the pattern to a OrmoComp UV resist layer, deposited on a PET substrate. The $MAPbI_3$ layer was then deposited by ink-jet printing of a precursor solution in DMSO. The final device showed again single mode lasing under 1 ns pumping at 532 nm, with a threshold of 270 μJcm^{-2}, and a linewidth of 0.4 nm, both about 2 times higher than the ones of the laser realized by spin coating.

The combination of NIL and ion beam milling (IBM), together with a proper choice of the imprint resist in order to allow its deposition on top of the perovskite layers, was used to realize an array

of micro-DFB lasers, exploiting $MAPbI_3$ as active material [72] with a lasing threshold of about 225 μJcm^{-2} under 5 ns pumping at 532 nm. Similar threshold, but under 300 ps pumping at 532 nm, were recently obtained in $MAPbI_3$ DFB lasers realized by solution deposition on imprinted plastic substrates, by using as precursor lead acetate ($Pb(CH_3COO)_2$), instead that PbI_2 [73].

DFB lasing in the green spectral region with a 1D pattern was reported for the first time by Pourdavoud et al. [66] with a $MAPbBr_3$ active film, directly imprinted by thermal nanoimprinting (see Figure 11a). The authors demonstrated an evident improvement of the film cristallinity and morphology due to the application of high pressure (100 bar) and temperature (100 °C), even when flat stamps were used, that allowed to obtain single mode lasing at about 555 nm with a remarkably low threshold of 3.4 μJcm^{-2}, and linewidth of 0.14 nm, under 300 ps pumping at 532 nm.

The search of high operational stability of the lasers also stimulated the development of fully inorganic perovskites with optical gain. Single mode emission at 654 nm was reported in $CsPbBrI_2$ films [74], spin coated on nanoimprinted polymer substrates, but no lasing was claimed by the authors, due to a particularly high linewidth of about 5 nm.

Clear single mode lasing in the green was instead very recently demonstrated from $CsPbBr_3$ thin films by Pourdavoud et al. [24], who optimized the film morphology, crystallinity and photoluminescence quantum yield (PLQY) by thermal imprinting. The DFB lasing properties were investigated in samples realized both by direct imprinting of the active layer and by deposition on an imprinted substrate, achieving in both cases a low lasing threshold of 10.0 μJcm^{-2} and 7.2 μJcm^{-2}, respectively, under 300 ps pumping at 355 nm.

A further degree of freedom for the optimization of the DFB lasing properties is the dimensionality of the nanopatterning used to introduce the interference necessary for the lasing feedback. In particular, a DFB laser exploiting a bidimensional pattern of nanopillars (see Figure 11f) was obtained in $MAPbI_3$ thin films both by Chen et al. [75] and by Whitworth et al. [68], obtaining single mode emission around 785 nm, with a linewidth of below 0.4 nm.

Furthermore, the last group also realized the only, to date, perovskite 2D DFB laser operating in the green by exploiting $MAPbBr_3$ as active material. After a proper optimization of the film realization procedure by solution, in order to minimize the ASE threshold, single mode lasing was demonstrated at about 555 nm, with a remarkably low threshold of 6 μJcm^{-2} under 1 ns pulsed pumping at 355 nm. Moreover, by acting on the grating period the authors demonstrated lasing from both TE and TM modes (see Figure 11d,e) [18].

Dual mode lasing was also obtained in 3D inverse opals of $MAPbBr_3$, realized by infiltration of a polystyrene opal with the perovskite precursor solution, followed by polystyrene dissolution in toluene [69] (see Figure 11g). In this case, a rather high threshold of 1.6 $mJcm^{-2}$ was found, under 500 ps pumping at 532 nm, thus much higher than the typical values of DFB perovskite lasers. This was probably due to a lower effective gain resulting from the low perovskite fraction in the inverse opal structure, or to higher scattering caused by the irregularities of the all-solution processed 3D photonic crystal structure, or to higher non radiative relaxation rate related to the high surface area of the inverse opal structure.

An interesting hybrid between DFB structures and WGM lasersg was demonstrated by depositing $MAPbBr_3$ microwires on a silicon grating [70] (see Figure 11h). In this case, single mode lasing was ascribed to the light confinement only in the microwires region above the void region, thus making the structure an array of microcavities, emitting along the substrate patterning direction.

Finally, DFB lasers with CW operation was recently reported in a device exploiting a $MAPbI_3$ thin film deposited on a patterned thin alumina layer on a high thermal conductivity sapphire substrate [7]. Linearly polarized single mode lasing was obtained at the specific temperature of 102 K, and ascribed to the gain from tetragonal phase inclusions that are photogenerated by the pump source within the normally existing orthorhombic matrix, with a clear threshold at 17 $KWcm^{-2}$, under CW pumping at 445 nm.

More recently room temperature lasing was claimed in a directly imprinted $MAPbI_3$ film showing the appearance of a narrow peak with a linewidth of 0.7 nm at high excitation density, ascribed to lasing with an extremely low threshold of only 13 Wcm^{-2} [76,77], under CW pumping at 355 nm.

3.4. Vertical Cavity Surface Emitting Lasers (VCSELs)

VCSELs are basically made by an active film cladded between two parallel highly reflecting mirrors. This kind of cavity allows to obtain laser beam with lower divergence, lower threshold and better quality with respect to DFBs and, for thin enough active layers, single mode emission. However as the lasing wavelength is dependent on the active layer thickness and the lasing feedback is given by multiple reflection in direction perpendicular to the mirrors, a good control of the active layer morphology and optical quality is fundamental to realize VCSELs. Moreover, the propagation losses in the cavity strongly depend on the mirrors reflectivity and absorption, thus requiring the use of two highly reflecting dielectric mirrors (Distributed Bragg Reflectors, DBR) for the losses minimization. The first perovskite VCSEL was demonstrated in 2014 by realizing a hybrid dielectric-metallic cavity made by a bottom DBR, a 200 nm-thick spin coated $MAPbI_{3-x}Cl_x$ active layer, a 1 µm-PMMA layer acting as spacer and a thermally evaporated 200 nm-thick top gold layer, acting as second mirror [6].

The microcavity emission spectra showed three modes at low excitation density and an almost single mode emission at high excitation densities due to the amplification of the mode at 775 nm (1.60 eV) (see Figure 12a). A lasing threshold of 0.2 µJ per pulse was reported (the absence of indications on the pump spot size prevents to determine the corresponding energy density), under 400 ps pumping at 532 nm.

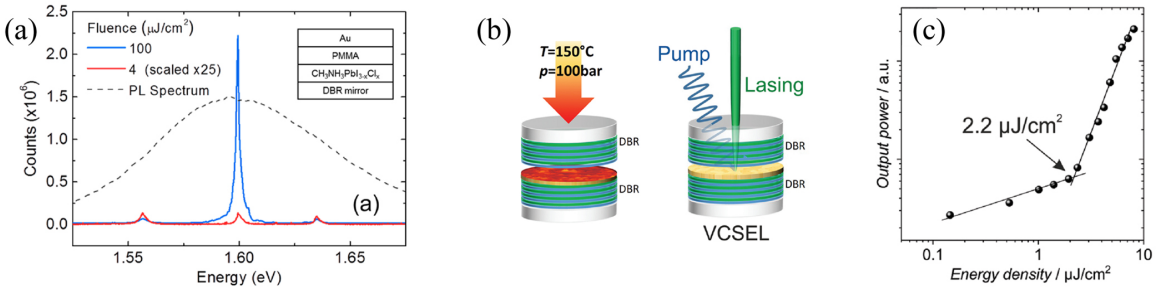

Figure 12. (**a**) Emission spectra of the $MAPbI_{3-x}Cl_x$ and of the VCSEL below and above the lasing threshold. Inset: scheme of the cavity structure. Reproduced with permission from [6]. American Chemical Society, 2014. (**b**) Pictorial view of the $CsPbBr_3$ VCSEL realization by thermal imprinting and of the VCSEL pumping and lasing. (**c**) Excitation density dependence of the emission intensity of the same sample, providing evidence of the lasing threshold. (**b**) and (**c**) adapted with permission from [24]. John Wiley and Sons, 2019.

This first result was followed by further VCSELs demonstrators only after three years, with the first report of perovskite VCSELs exploiting two DBR mirrors and $MAPbI_3$ as active material [78]. The active layer was deposited by spin coating of a precursor solution on the bottom DBR covered by a PPMA layer, followed by toluene dripping. The careful optimization of the precursor solvent selection, the molar ratio of precursors, the toluene dripping timing protocol, the thermal annealing temperature and duration, and the treatment of substrate surface to make it hydrophilic, showed the extreme importance of good optical quality of the VCSELs active layer. The full cavity was mechanically assembled by bonding the top DBR above the perovskite film with wafer edges sealed with optical epoxy, also depositing a 10 nm-thin PMMA layer on the perovskite film before applying the top DBR bonding process. The laser showed single mode emission at 778.4 nm, with a threshold of 7.6 μJcm^{-2}, with TEM_{00} lasing and low divergence (<3°) under 340 ps pulses pumping at 532 nm, and with a threshold of about 114 μJcm^{-2} under 5 ns pulses pumping at the same pumping wavelength.

Fully dielectric cavities assembled by gluing the top mirror on the active layer were also reported in devices exploiting as active layer a $CsPbBr_3$ nanocrystals thin film [79], showing single mode lasing with a threshold as low as 0.39 μJcm^{-2} under 50 fs pulses pumping at 400 nm and of 98 μJcm^{-2} under 5 ns pulses pumping at 355 nm.

The importance of the quality of the mirrors in determining the VCSEL lasing properties is clearly demonstrated by the results obtained in DBR-metal cavities with a $MAPbI_3$ active layer [80]. Even if the active layer is expected to be nominally comparable with the one in Ref. [78] this second laser only showed lasing at cryogenic temperatures (below 75 K).

Thus the development of approaches allowing the realization of VCSELs with both top and bottom DBR mirrors is fundamental to optimize the lasing properties. An interesting approach was developed by the group of Prof. Nurmikko, who realized monolithic DBR-perovskite-DBR cavities operating in the green by directly depositing the top DBR on the active layer by sputtering, by using both $FAPbBr_3$ [81] and mixed cation $Cs_{0.13}FA_{0.87}PbBr_3$ [82] as active materials.

A last example of fully dielectric perovskite VCSELs was recently reported by Pourdavoud et al. [24] that used the top DBR mirror as stamp for a $CsPbBr_3$ thin film deposited on the bottom mirror in a thermal imprinting process, leaving the stamp attached to the perovskite layer (see Figure 12b). This experiment is particularly interesting as it allows a direct comparison with state of the art DFB lasers, realized in the same experiment, with the same active layer. The VCSEL showed a single mode at 538 nm, with a threshold of 2.2 μJcm^{-2} and a linewidth of 0.07 nm (resolution limited), 3.3 and 2 times lower than the threshold and linewidth of the DFB laser, respectively (see Figure 12c), under 340 ps pumping at 355 nm.

Finally, fully spin coated microcavities were recently demonstrated by Lova et al. [83] that deposited a bottom DBR by spin coating of alternated layers of poly(N-vinylcarbazole) and cellulose acetate dissolved in orthogonal solvents, a protecting perfluorinated polymer layer, a further PVK layer, a $MAPBI_3$ layer and, finally, a symmetric top mirror. Even if no lasing was reported from the sample the authors demonstrated enhanced PL intensity in correspondence of the cavity modes, proposing this technique for future experiments on perovskite VCSELs. The main data on all the discussed results are summarized in Table 2.

Table 2. Lasing properties of the perovskite lasers described in this review. The data are grouped taking into account the active material and then the cavity type, and are in order of increasing pump pulse time width. In papers discussing multiple devices the reported data are relative to the device with the minimum threshold. N/A evidences non available data.

Active Material	Cavity Geometry	Threshold	Peak wav. (nm)	Pump Pulse Length	Pump wav. (nm)	Ref.
$MAPbI_3$	random	11 μJcm^{-2}	≈780	400 ps	532	[42]
$MAPbI_3$	random	230 μJcm^{-2} (77 K)	≈745	0.5 ns	335	[41]
$MAPbI_3$	random	200 μJcm^{-2}	≈784	0.8 ns	335	[39]
$MAPbI_3$	random	102 μJcm^{-2}	≈775	1.0 ns	335	[40]
$MAPbI_3$ microhexagons	WGM	9 μJcm^{-2}	≈782	50 fs	400	[58]
$MAPbI_3$ microtriangle	WGM	37 μJcm^{-2}	≈760	50 fs	400	[48]
$MAPbI_3$ microsphere	WGM	75 μJcm^{-2} (80 K)	≈755	2 ns	355	[62]
$MAPbI_3$	DFB	228 μJcm^{-2}	789.5	300 ps	532	[73]
$MAPbI_3$	DFB	120 μJcm^{-2}	786.5	1 ns	532	[67]
$MAPbI_3$	DFB	270 μJcm^{-2}	784	1 ns	532	[71]
$MAPbI_3$	DFB	225 μJcm^{-2}	784.3	5 ns	532	[72]
$MAPbI_3$	2D-DFB	4 μJcm^{-2}	784	200 fs	515	[68]
$MAPbI_3$	2D-DFB	68.5 μJcm^{-2}	788	270 ps	532	[75]
$MAPbI_3$	2D-DFB	110 μJcm^{-2}	784	910 ps	355	[68]
$MAPbI_3$	DBR-DBR VCSEL	7.6 μJcm^{-2}	778.4	340 ps	532	[78]
$MAPbI_3$	DBR-DBR VCSEL	114 μJcm^{-2}	778.4	5 ns	532	[78]
$MAPbI_{3-x}Cl_x$	DBR-metal VCSEL	0.2 μJ	775	400 ps	532	[6]
$MAPbBr_3$ NCs	random	1 $nJcm^{-2}$	≈540	55 ps	374	[46]
$MAPbBr_3$ NCs	random	10 μJcm^{-2}	≈540	N/A	374	[44]
$MAPbBr_3$ microwire	WGM	2.37 μJcm^{-2}	558.5	100 fs	400	[55]
$MAPbBr_3$ microcube	WGM	290.7 μJcm^{-2}	≈555	100 fs	405	[57]
$MAPbBr_3$ microcystals	WGM	3.6 μJcm^{-2}	557.5	120 fs	400	[53]
$MAPbBr_3$ microcapillary	WGM	4.7 μJcm^{-2}	560	200 fs	397	[64]
$MAPbBr_3$ microdisks	WGM	30 μJcm^{-2}	≈550	200–300 fs	397	[51]
$MAPbBr_3$ Fabry-Perot	WGM	150 μJcm^{-2}	≈550	200–300 fs	397	[52]
$MAPbBr_3$	DFB	3.4 μJcm^{-2}	555.3	300 ps	532	[66]
$MAPbBr_3$	2D-DFB	6 μJcm^{-2}	547	1 ns	355	[18]
$MAPbBr_3$	3D opal	1.6 $mJcm^{-2}$	544.56–545.54	500 ps	532	[69]
$BAMAPbBrCsPbCl_3$ microring	WGM	12.2 μJcm^{-2}	≈542	150 fs	400	[60]

Table 2. *Cont.*

Active Material	Cavity Geometry	Threshold	Peak wav. (nm)	Pump Pulse Length	Pump wav. (nm)	Ref.
$FAPbBr_3$	DBR-DBR VCSEL	18.3 μJcm^{-2}	552.4	340 ps	355	[81]
$Cs_{0.13}FA_{0.87}PbBr_3$	DBR-DBR VCSEL	13.5 μJcm^{-2}	552.5	340 ps	355	[79]
$CsPbBr_3$-ZnO	random (ASE)	207 μJcm^{-2}	≈565	50 fs	400	[43]
$CsPbBr_3$ microsphere	WGM	0.42 μJcm^{-2}	545	40 fs	400	[63]
$CsPbBr_3$ microsquare	WGM	2.2 μJcm^{-2}	≈536	50 fs	400	[49]
$CsPbBr_3$ microcube	WGM	16.9 μJcm^{-2}	541	80 fs	470	[56]
$CsPbBr_3$ microwire	WGM	5.0 μJcm^{-2}	≈535	100 fs	400	[54]
$CsPbBr_3$ microwire	WGM	2.2 μJcm^{-2}	≈546	N/A fs	355	[61]
$CsPbBr_3$ microcube	WGM	214 μJcm^{-2}	536.8	1.1 ns	355	[56]
$CsPbBr_3$ microsquare	WGM	16.7 μJcm^{-2}	≈534	N/A	355	[50]
$CsPbBr_3$	DFB	7.2 μJcm^{-2}	539.1	300 ps	355	[24]
$CsPbBr_3$	DBR-DBR VCSEL	2.2 μJcm^{-2}	538	300 ps	355	[24]
$CsPbCl_3$ microsquare	WGM	5 μJcm^{-2}	≈427	150 fs	400	[59]
$CsPbCl_3$ microsquare	WGM	32 μJcm^{-2}	≈425	N/A	355	[50]
$CsPbI_3$ microsquare	WGM	28.4 μJcm^{-2}	≈709	N/A	355	[50]
$CsPbBr_3$ NCs	DBR-DBR VCSEL	0.39 μJcm^{-2}	522	50 fs	400	[79]
$CsPbBr_3$ NCs	DBR-DBR VCSEL	98 μJcm^{-2}	522	5 ns	355	[79]

4. Applicative Perspectives

4.1. Pumping Regime

A first important aspect to consider in order to evaluate the possibilities to build a real laser from a given active material is the pumping temporal regime necessary to have optical gain and lasing. By looking at the 73 results reported in Tables 1 and 2 relative to room temperature data and with specified pump pulse time length (among the 80 in total) it can be observed than only 20 (about 27%) were obtained by using pump pulses not shorter than 1 nanosecond, while about 50% of the experiments were performed with ultrafast pumping (between 50 fs and 300 fs).

To quantitatively investigate the role of the pump pulse temporal length on the ASE and lasing properties we can compare the experimental results obtained in the literature in the actually few experiments in which the same active material is investigated by using both ultrafast (fs) and quasi-CW (ns) excitation, thus allowing a direct threshold comparison between the two regimes (see Table 1).

Concerning ASE experiments Wu et al. [15] demonstrated a threshold increase of about 1.7 times and 2 times when passing from 120 fs- to 7 ns-pumping in $MAPbI_3$ and in $MAPbI_3$-PMMA films, respectively. Larger differences were instead observed in $FAPbI_3$ thin films [21], showing an ASE increase of 6.5 times under nanosecond pumping, and in state of the art $CsPbBr_3$ thin films deposited by one step coevaporation [23]) providing evidence of an ASE threshold under nanosecond pumping about 20 times higher than under femtosecond pumping. Finally, Yakunin et al. [5] observed a threshold of 450 μJcm^{-2} in $CsPbBr_3$ NCs films pumped by 10 ns pulses, thus 85 times higher than the one under 100 fs pumping (5.3 μJcm^{-2}).

Concerning lasers to date only three examples of pumping in both regimes are present, providing evidence of qualitatively similar higher thresholds under nanosecond pumping than under femtosecond pumping, but with higher quantitative variation with respect to the results on ASE. In particular, a threshold increase of 15 times was demonstrated in $MAPbI_3$ VCSEL [78] passing from 340 ps to 5 ns pump pulses, while a higher variation (27.5 times) was obtained in $MAPbI_3$ 2-D DFB VCSEL [68] passing from 200 fs to 910 ps. Much higher differences were observed in $CsPbBr_3$ NCs films used in a VCSEL laser, with a threshold increase of 250 times between excitation with 50 fs- and 5 ns-lasers [79].

By looking at these data and considering that femtosecond pumping typically also results in higher damage threshold and higher photostability, it could be ingenuously concluded that femtosecond pumping is better than nanosecond pumping. Anyway on an applicative perspective this conclusion is wrong as the generation of ultrafast and highly energetic pulses requires big and expensive amplified pump lasers, not suitable for the excitation of any realistic compact and low cost laser device. On the contrary nanosecond pulses can be obtained by compact and low cost laser diodes and, eventually, also by inorganic LEDs that could be exploited for the realization of compact optically pumped perovskite lasers, as already demonstrated for optically pumped organic lasers [84].

Thus the investigation of the ASE and lasing threshold and of their intensity stability under nanosecond optical excitation is more suitable to reproduce the possible working conditions of optically pumped perovskite lasers exploiting cheap and compact pumping sources.

4.2. Toward Electrically Pumped Lasers

The demonstration of ASE and lasing under nanosecond pumping, together with the rapid evolution of the performances of perovskites LEDs [3], of course stimulate the interest toward electrically driven perovskite-based laser diodes. Despite the possibility to drive LEDs with nanosecond voltage pulses this target seems currently extremely ambitious if one compares the excitation regime needed for lasing with the current densities demonstrated to date in LEDs. For example Leyden et al. [85] recently investigated the lasing properties of 2D-perovskites, demonstrating single mode lasing with a threshold of 7 μJcm^{-2} under 800 ps optical pumping, corresponding to a power density of about 9 $kWcm^{-2}$. Starting from these values they estimated a current density for lasing under electrical excitation of the order of 4–10 $kAcm^{-2}$ and compared it with

the performances of a LED driven by 500 ns voltage pulses. The LED demonstrated failure starting from about 200 Acm^{-2}, which is at least 20 times smaller than the estimated current density for the lasing threshold. This result clearly shows that much work has still to be done to lead perovskite LEDs to the current density regimes required for lasing, to properly improve the heat dissipation and the charge balance, and to successfully integrate the electrodes with the active material preserving the optical gain properties.

4.3. Toward Cheap Optically Pumped Lasers

Even if the target of electrically driven perosvkite lasers actually still seems particularly ambitious, it is interesting to observe that cheap and compact laser devices could be more simply realized by exploiting suitable sources of pulsed light. Several interesting works were performed in the last two decades in order to develop these kinds of devices with organic active materials, successfully demonstrating the progressive transition of the pump source from the initial ultrafast lasers [86], to microchip Q-switched lasers [87], to UV laser diodes [88] and, finally, to UV LEDs [89].

Among the available results on optically pumped perovskite lasers the lowest threshold power density of 1 $kWcm^{-2}$ was obtained in 2D-DFB with a $MAPbBr_3$ active layer [18]. This value is actually pretty close to the maximum power density (840 Wcm^{-2}) of the pulsed UV LEDs and about 4 times smaller that the maximum power density of the UV pulsed laser diodes used to date to optically pump organic DFB lasers [88,90]. Considering the possibility to further improve the DFB resonators, for example with mixed order gratings, and the rapid threshold decrease of perovskites lasers, we could expect the demonstration of compact optically pumped perovskite laser prototypes in short times.

Author Contributions: M.L.D.G. and M.A. equally contributed to the organization and writing of the paper.

Funding: This research received no external funding.

Conflicts of Interest: The authors declare no conflict of interest.

References

1. Kojima, A.; Teshima, K.; Shirai, Y.; Miyasaka, T. Organometal Halide Perovskites as Visible-Light Sensitizers for Photovoltaic Cells. *J. Am. Chem. Soc.* **2009**, *131*, 6050–6051. [CrossRef] [PubMed]
2. National Renewable Energy Laboratory. Research Cell Record Efficiency Chart. Available online: https://www.nrel.gov/pv/assets/pdfs/best-reserch-cell-efficiencies.pdf (accessed on 8 October 2019).
3. Van Le, Q.; Jang, H.W.; Kim, S.Y. Recent Advances toward High-Efficiency Halide Perovskite Light-Emitting Diodes: Review and Perspective. *Small Methods* **2018**, *2*, 1700419. [CrossRef]
4. Xing, G.; Nripan, M.; Lim, S.S.; Yantara, N.; Liu, X.; Sabba, D.; Grätzel, M.; Mhaisalkar, S.; Sum, T.C. Low-Temperature Solution-Processed Wavelength-Tunable Perovskites for Lasing. *Nat. Mater.* **2014**, *13*, 476–480. [CrossRef] [PubMed]
5. Yakunin, S.; Protesescu, L.; Krieg, F.; Bodnarchuk, M.I.; Nedelcu, G.; Humer, M.; De Luca, G.; Fiebig, M.; Heiss, W.; Kovalenko, M.V. Low-Threshold Amplified Spontaneous Emission and Lasing From Colloidal Nanocrystals of Caesium Lead Halide Perovskites. *Nat. Commun.* **2015**, *6*, 8056. [CrossRef]
6. Deschler, F.; Price, M.; Pathak, S.; Klintberg, L.E.; Jarausch, D.D.; Higler, R.; Hüttner, S.; Leijtens, T.; Stranks, S.D.; Snaith, H.J.; et al. High Photoluminescence Efficiency and Optically Pumped Lasing in Solution-Processed Mixed Halide Perovskite Semiconductors. *J. Phys. Chem. Lett.* **2014**, *5*, 1421–1426. [CrossRef]
7. Jia, Y.; Kerner, R.A.; Grede, A.J.; Rand, B.P.; Giebink, N.C. Continuous-wave lasing in an organic-inorganic lead halide perovskite semiconductor. *Nat. Photonics* **2017**, *11*, 784–788. [CrossRef]
8. Kondo, S.; Suzuki, K.; Saito, T.; Asada, H.; Nakagawa, H. Photoluminescence and stimulated emission from microcrystalline $CsPbCl_3$ films prepared by amorphous-to-crystalline transformation. *Phys. Rev. B* **2004**, *70*, 205322. [CrossRef]
9. Kondo, S.; Suzuki, K.; Saito, T.; Asada, H.; Nakagawa, H. Confinement-enhanced stimulated emission in microcrystalline CsPbCl3 films grown from the amorphous phase. *J. Cryst. Growth* **2005**, *282*, 94–104. [CrossRef]

10. Kondo, S.; Ohsawa, H.; Saito, T.; Asada, H.; Nakagawa, H. Room-temperature stimulated emission from microcrystalline CsPbCl3 films. *Appl. Phys. Lett.* **2005**, *87*, 131912. [CrossRef]
11. Kondo, S.; Takahashi, K.; Nakanish, T.; Saito, T.; Asada, H.; Nakagawa, H. High intensity photoluminescence of microcrystalline CsPbBr3 films: Evidence for enhanced stimulated emission at room temperature. *Curr. Appl. Phys.* **2007**, *7*, 1–5. [CrossRef]
12. Stranks, S.D.; Wood, S.M.; Wojciechowski, K.; Deschler, F.; Saliba, M.; Khandelwal, H.; Patel, J.B.; Elston, S.J.; Herz, L.M.; Johnston, M.B.; et al. Enhanced Amplified Spontaneous Emission in Perovskites Using a Flexible Cholesteric Liquid Crystal Reflector. *Nano Lett.* **2015**, *15*, 4935–4941. [CrossRef] [PubMed]
13. Li, J.; Si, J.; Gan, L.; Liu, Y.; Ye, Z.; He, H. Simple Approach to Improving the Amplified Spontaneous Emission Properties of Perovskite Films. *ACS Appl. Mater. Interfaces* **2016**, *8*, 32978–32983. [CrossRef] [PubMed]
14. Lampert, Z.E.; Papanikolas, J.M.; Lewis Reynolds, C. Enhancement of optical gain and amplified spontaneous emission due to waveguide geometry in the conjugated polymer poly[2-methoxy-5-(2′-ethylhexyloxy)-p-phenylene vinylene]. *Appl. Phys. Lett.* **2013**, *102*, 073303. [CrossRef]
15. Wu, X.; Jiang, X.F.; Hu, X.; Zhang, D.F.; Li, S.; Yao, X.; Liu, W.; Yip, H.L.; Tang, Z.; Xu, Q.H. Highly stable enhanced near-infrared amplified spontaneous emission in solution-processed perovskite films by employing polymer and gold nanorods. *Nanoscale* **2019**, *11*, 1959–1967. [CrossRef]
16. Qin, L.; Lv, L.; Ning, Y.; Li, C.; Lu, Q.; Zhu, L.; Hu, Y.; Lou, Z.; Teng, F.; Hou, Y. Enhanced amplified spontaneous emission from morphology-controlled organic–inorganic halide perovskite films. *RSC Adv.* **2015**, *5*, 103674–103679. [CrossRef]
17. Lafalce, E.; Zhang, C.; Zhai, Y.; Sun, D.; Vardeny, Z.V. Enhanced emissive and lasing characteristics of nano-crystalline MAPbBr3 films grown via anti-solvent precipitation. *J. Appl. Phys.* **2016**, *120*, 143101. [CrossRef]
18. Harwell, J.R.; Whitworth, G.L.; Turnbull, G.A.; Samuel, I.D.W. Green Perovskite Distributed Feedback Lasers. *Sci. Rep.* **2017**, *7*, 11727. [CrossRef]
19. Ngo, T.T.; Suarez, I.; Antonicelli, G.; Cortizo-Lacalle, D.; Martinez-Pastor, J.P.; Mateo-Alonso, A.; Mora-Sero, I. Enhancement of the Performance of Perovskite Solar Cells, LEDs, and Optical Amplifiers by Anti-Solvent Additive Deposition. *Adv. Mater.* **2017**, *29*, 1604056. [CrossRef]
20. Matsushima, T.; Inoue, M.; Fujihara, T.; Terakawa, S.; Qin, C.; Sandanayaka, A.S.; Adachi, C. High-coverage organic-inorganic perovskite film fabricated by double spin coating for improved solar power conversion and amplified spontaneous emission. *Chem. Phys. Lett.* **2016**, *661*, 131–135. [CrossRef]
21. Yuan, F.; Wu, Z.; Dong, H.; Xi, J.; Xi, K.; Divitini, G.; Jiao, B.; Hou, X.; Wang, S.; Gong, Q. High Stability and Ultralow Threshold Amplified Spontaneous Emission from Formamidinium Lead Halide Perovskite Films. *J. Phys. Chem. C* **2017**, *121*, 15318–15325. [CrossRef]
22. De Giorgi, M.L.; Perulli, A.; Yantara, N.; Boix, P.P.; Anni, M. Amplified Spontaneous Emission Properties of Solution Processed CsPbBr3 Perovskite Thin Films. *J. Phys. Chem. C* **2017**, *121*, 14772–14778. [CrossRef]
23. Zhang, L.; Yuan, F.; Dong, H.; Jiao, B.; Zhang, W.; Hou, X.; Wang, S.; Gong, Q.; Wu, Z. One-Step Co-Evaporation of All-Inorganic Perovskite Thin Films with Room-Temperature Ultralow Amplified Spontaneous Emission Threshold and Air Stability. *ACS Appl. Mater. Interfaces* **2018**, *10*, 40661–40671. [CrossRef] [PubMed]
24. Pourdavoud, N.; Haeger, T.; Mayer, A.; Cegielski, P.J.; Giesecke, A.L.; Heiderhoff, R.; Olthof, S.; Zaefferer, S.; Shutsko, I.; Henkel, A.; et al. Room-Temperature Stimulated Emission and Lasing in Recrystallized Cesium Lead Bromide Perovskite Thin Films. *Adv. Mater.* **2019**, *31*, 1903717. [CrossRef] [PubMed]
25. Brenner, P.; Bar-On, O.; Jakoby, M.; Allegro, I.; Richards, B.S.; Paetzold, U.W.; Howard, I.A.; Scheuer, J.; Lemmer, U. Continuous wave amplified spontaneous emission in phase-stable lead halide perovskites. *Nat. Commun.* **2019**, *10*, 988. [CrossRef]
26. Fan, F.; Voznyy, O.; Sabatini, R.P.; Bicanic, K.T.; Adachi, M.M.; McBride, J.R.; Reid, K.R.; Park, Y.S.; Li, X.; Jain, A.; et al. Continuous wave lasing in colloidal quantum dot solids enabled by facet selective epitaxy. *Nature* **2017**, *544*, 75–79. [CrossRef]
27. Hide, F.; Diaz-Garcia, M.; Schwartz, B.; Andersson, M.; Pei, Q.; Heeger, A. Semiconducting Polymers: A New Class of Solid-State Laser Materials. *Science* **1996**, *273*, 1833–1836.

28. Protesescu, L.; Yakunin, S.; Bodnarchuk, M.I.; Krieg, F.; Caputo, R.; Hendon, C.H.; Yang, R.X.; Walsh, A.; Kovalenko, M.V. Nanocrystals of Cesium Lead Halide Perovskites (CsPbX3, X = Cl, Br, and I): Novel Optoelectronic Materials Showing Bright Emission with Wide Color Gamut. *Nano Lett.* **2015**, *15*, 3692–3696. [CrossRef]
29. Wang, Y.; Li, X.; Song, J.; Xiao, L.; Zeng, H.; Sun, H. All-Inorganic Colloidal Perovskite Quantum Dots: A New Class of Lasing Materials with Favorable Characteristics. *Adv. Mater.* **2015**, *27*, 7101–7108. [CrossRef]
30. Balena, A.; Perulli, A.; Fernandez, M.; De Giorgi, M.L.; Nedelcu, G.; Kovalenko, M.V.; Anni, M. Temperature Dependence of the Amplified Spontaneous Emission from CsPbBr3 Nanocrystal Thin Films. *J. Phys. Chem. C* **2018**, *122*, 5813–5819. [CrossRef]
31. Vybornyi, O.; Yakunin, S.; Kovalenko, M.V. Polar-solvent-free colloidal synthesis of highly luminescent alkylammonium lead halide perovskite nanocrystals. *Nanoscale* **2016**, *8*, 6278–6283. [CrossRef]
32. Protesescu, L.; Yakunin, S.; Bodnarchuk, M.I.; Bertolotti, F.; Masciocchi, N.; Guagliardi, A.; Kovalenko, M.V. Monodisperse Formamidinium Lead Bromide Nanocrystals with Bright and Stable Green Photoluminescence. *J. Am. Chem. Soc.* **2016**, *138*, 14202–14205. [CrossRef] [PubMed]
33. Protesescu, L.; Yakunin, S.; Kumar, S.; Bär, J.; Bertolotti, F.; Masciocchi, N.; Guagliardi, A.; Grotevent, M.; Shorubalko, I.; Bodnarchuk, M.I.; et al. Dismantling the "Red Wall" of Colloidal Perovskites: Highly Luminescent Formamidinium and Formamidinium-Cesium Lead Iodide Nanocrystals. *ACS Nano* **2017**, *11*, 3119–3134. [CrossRef] [PubMed]
34. Papagiorgis, P.; Manoli, A.; Protesescu, L.; Achilleos, C.; Violaris, M.; Nicolaides, K.; Trypiniotis, T.; Bodnarchuk, M.I.; Kovalenko, M.V.; Othonos, A.; et al. Efficient Optical Amplification in the Nanosecond Regime from Formamidinium Lead Iodide Nanocrystals. *ACS Photonics* **2018**, *5*, 907–917. [CrossRef]
35. Krieg, F.; Ochsenbein, S.T.; Yakunin, S.; ten Brinck, S.; Aellen, P.; Süess, A.; Clerc, B.; Guggisberg, D.; Nazarenko, O.; Shynkarenko, Y.; et al. Colloidal CsPbX3 (X = Cl, Br, I) Nanocrystals 2.0: Zwitterionic Capping Ligands for Improved Durability and Stability. *ACS Energy Lett.* **2018**, *3*, 641–646. [CrossRef] [PubMed]
36. Yan, D.; Shi, T.; Zang, Z.; Zhou, T.; Liu, Z.; Zhang, Z.; Du, J.; Leng, Y.; Tang, X. Ultrastable CsPbBr3 Perovskite Quantum Dot and Their Enhanced Amplified Spontaneous Emission by Surface Ligand Modification. *Small* **2019**, *15*, 1901173. [CrossRef] [PubMed]
37. Veldhuis, S.A.; Tay, Y.K.E.; Bruno, A.; Dintakurti, S.S.H.; Bhaumik, S.; Muduli, S.K.; Li, M.; Mathews, N.; Sum, T.C.; Mhaisalkar, S.G. Benzyl Alcohol-Treated CH3NH3PbBr3 Nanocrystals Exhibiting High Luminescence, Stability, and Ultralow Amplified Spontaneous Emission Thresholds. *Nano Lett.* **2017**, *17*, 7424–7432. [CrossRef] [PubMed]
38. Wang, S.; Yu, J.; Zhang, M.; Chen, D.; Li, C.; Chen, R.; Jia, G.; Rogach, A.L.; Yang, X. Stable, Strongly Emitting Cesium Lead Bromide Perovskite Nanorods with High Optical Gain Enabled by an Intermediate Monomer Reservoir Synthetic Strategy. *Nano Lett.* **2019**, *19*, 6315–6322. [CrossRef]
39. Dhanker, R.; Brigeman, A.N.; Larsen, A.V.; Stewart, R.J.; Asbury, J.B.; Giebink, N.C. Random lasing in organo-lead halide perovskite microcrystal networks. *Appl. Phys. Lett.* **2014**, *105*, 151112. [CrossRef]
40. Shi, Z.F.; Sun, X.G.; Wu, D.; Xu, T.T.; Tian, Y.T.; Zhang, Y.T.; Li, X.J.; Du, G.T. Near-infrared random lasing realized in a perovskite CH3NH3PbI3 thin film. *J. Mater. Chem. C* **2016**, *4*, 8373–8379. [CrossRef]
41. Kao, T.S.; Chou, Y.H.; Hong, K.B.; Huang, J.F.; Chou, C.H.; Kuo, H.C.; Chen, F.C.; Lu, T.C. Controllable lasing performance in solution-processed organic-inorganic hybrid perovskites. *Nanoscale* **2016**, *8*, 18483–18488. [CrossRef]
42. Safdar, A.; Wang, Y.; Krauss, T.F. Random lasing in uniform perovskite thin films. *Opt. Express* **2018**, *26*, A75–A84. [CrossRef] [PubMed]
43. Li, C.; Zang, Z.; Han, C.; Hu, Z.; Tang, X.; Du, J.; Leng, Y.; Sun, K. Highly compact CsPbBr3 perovskite thin films decorated by ZnO nanoparticles for enhanced random lasing. *Nano Energy* **2017**, *40*, 195–202. [CrossRef]
44. Hu, H.W.; Haider, G.; Liao, Y.M.; Roy, P.K.; Ravindranath, R.; Chang, H.T.; Lu, C.H.; Tseng, C.Y.; Lin, T.Y.; Shih, W.H.; et al. Wrinkled 2D Materials: A Versatile Platform for Low-Threshold Stretchable Random Lasers. *Adv. Mater.* **2017**, *29*, 1703549. [CrossRef] [PubMed]
45. Anni, M.; Rhee, D.; Lee, W.K. Random Lasing Engineering in Poly-(9-9dioctylfluorene) Active Waveguides Deposited on Wrinkles Corrugated Surfaces. *ACS Appl. Mater. Interfaces* **2019**, *11*, 9385–9393. [CrossRef]

46. Roy, P.K.; Haider, G.; Lin, H.I.; Liao, Y.M.; Lu, C.H.; Chen, K.H.; Chen, L.C.; Shih, W.H.; Liang, C.T.; Chen, Y.F. Multicolor Ultralow-Threshold Random Laser Assisted by Vertical-Graphene Network. *Adv. Opt. Mater.* **2018**, *6*, 1800382. [CrossRef]
47. Liu, Y.; Yang, W.; Xiao, S.; Zhang, N.; Fan, Y.; Qu, G.; Song, Q. Surface-Emitting Perovskite Random Lasers for Speckle-Free Imaging. *ACS Nano* **2019**. [CrossRef]
48. Zhang, Q.; Ha, S.T.; Liu, X.; Sum, T.C.; Xiong, Q. Room-Temperature Near-Infrared High-Q Perovskite Whispering-Gallery Planar Nanolasers. *Nano Lett.* **2014**, *14*, 5995–6001. [CrossRef]
49. Zhang, Q.; Su, R.; Liu, X.; Xing, J.; Sum, T.C.; Xiong, Q. High-Quality Whispering-Gallery-Mode Lasing from Cesium Lead Halide Perovskite Nanoplatelets. *Adv. Funct. Mater.* **2016**, *26*, 6238–6245. [CrossRef]
50. Guo, P.; Hossain, M.K.; Shen, X.; Sun, H.; Yang, W.; Liu, C.; Ho, C.Y.; Kwok, C.K.; Tsang, S.W.; Luo, Y.; et al. Room-Temperature Red-Green-Blue Whispering-Gallery Mode Lasing and White-Light Emission from Cesium Lead Halide Perovskite (CsPbX3, X = Cl, Br, I) Microstructures. *Adv. Opt. Mater.* **2018**, *6*, 1700993. [CrossRef]
51. Sasaki, F.; Mochizuki, H.; Zhou, Y.; Sonoda, Y.; Azumi, R. Optical pumped lasing in solution processed perovskite semiconducting materials: Self-assembled microdisk lasing. *Jpn. J. Appl. Phys.* **2016**, *55*, 04ES02. [CrossRef]
52. Sasaki, F.; Mochizuki, H.; Zhou, Y.; Sonoda, Y.; Azumi, R. Optical pumped lasing in solution processed perovskite semiconducting materials: Self-assembled Fabry-Perot microcavity. *Jpn. J. Appl. Phys.* **2017**, *56*, 04CL07. [CrossRef]
53. Liao, Q.; Hu, K.; Zhang, H.; Wang, X.; Yao, J.; Fu, H. Perovskite Microdisk Microlasers Self-Assembled from Solution. *Adv. Mater.* **2015**, *27*, 3405–3410. [CrossRef] [PubMed]
54. Wang, S.; Wang, K.; Gu, Z.; Wang, Y.; Huang, C.; Yi, N.; Xiao, S.; Song, Q. Solution-Phase Synthesis of Cesium Lead Halide Perovskite Microrods for High-Quality Microlasers and Photodetectors. *Adv. Opt. Mater.* **2017**, *5*, 1700023. [CrossRef]
55. Wang, K.; Sun, S.; Zhang, C.; Sun, W.; Gu, Z.; Xiao, S.; Song, Q. Whispering-gallery-mode based CH3NH3PbBr3 perovskite microrod lasers with high quality factors. *Mater. Chem. Front.* **2017**, *1*, 477–481. [CrossRef]
56. Zhou, B.; Dong, H.; Jiang, M.; Zheng, W.; Sun, L.; Zhao, B.; Tang, B.; Pan, A.; Zhang, L. Single-mode lasing and 3D confinement from perovskite micro-cubic cavity. *J. Mater. Chem. C* **2018**, *6*, 11740–11748. [CrossRef]
57. Li, F.; Lu, J.; Zhang, Q.; Peng, D.; Yang, Z.; Xu, Q.; Pan, C.; Pan, A.; Li, T.; Wang, R. Controlled fabrication, lasing behavior and excitonic recombination dynamics in single crystal CH3NH3PbBr3 perovskite cuboids. *Sci. Bull.* **2019**, *64*, 698–704. [CrossRef]
58. Liu, X.; Niu, L.; Wu, C.; Cong, C.; Wang, H.; Zeng, Q.; He, H.; Fu, Q.; Fu, W.; Yu, T.; et al. Periodic Organic-Inorganic Halide Perovskite Microplatelet Arrays on Silicon Substrates for Room-Temperature Lasing. *Adv. Sci.* **2016**, *3*, 1600137. [CrossRef]
59. He, X.; Liu, P.; Zhang, H.; Liao, Q.; Yao, J.; Fu, H. Patterning Multicolored Microdisk Laser Arrays of Cesium Lead Halide Perovskite. *Adv. Mater.* **2017**, *29*, 1604510. [CrossRef]
60. Zhang, H.; Liao, Q.; Wu, Y.; Zhang, Z.; Gao, Q.; Liu, P.; Li, M.; Yao, J.; Fu, H. 2D Ruddlesden-Popper Perovskites Microring Laser Array. *Adv. Mater.* **2018**, *30*, 1706186. [CrossRef]
61. Yang, Z.; Lu, J.; ZhuGe, M.; Cheng, Y.; Hu, J.; Li, F.; Qiao, S.; Zhang, Y.; Hu, G.; Yang, Q.; et al. Controllable Growth of Aligned Monocrystalline CsPbBr3 Microwire Arrays for Piezoelectric-Induced Dynamic Modulation of Single-Mode Lasing. *Adv. Mater.* **2019**, *31*, 1900647. [CrossRef]
62. Sutherland, B.R.; Hoogland, S.; Adachi, M.M.; Wong, C.T.O.; Sargent, E.H. Conformal Organohalide Perovskites Enable Lasing on Spherical Resonators. *ACS Nano* **2014**, *8*, 10947–10952. [CrossRef] [PubMed]
63. Tang, B.; Dong, H.; Sun, L.; Zheng, W.; Wang, Q.; Sun, F.; Jiang, X.; Pan, A.; Zhang, L. Single-Mode Lasers Based on Cesium Lead Halide Perovskite Submicron Spheres. *ACS Nano* **2017**, *11*, 10681–10688. [CrossRef] [PubMed]
64. Kurahashi, N.; Nguyen, V.C.; Sasaki, F.; Yanagi, H. Whispering gallery mode lasing in lead halide perovskite crystals grown in microcapillary. *Appl. Phys. Lett.* **2018**, *113*, 011107. [CrossRef]
65. Zhang, N.; Sun, W.; Rodrigues, S.P.; Wang, K.; Gu, Z.; Wang, S.; Cai, W.; Xiao, S.; Song, Q. Highly Reproducible Organometallic Halide Perovskite Microdevices based on Top-Down Lithography. *Adv. Mater.* **2017**, *29*, 1606205. [CrossRef] [PubMed]

66. Pourdavoud, N.; Mayer, A.; Buchmüller, M.; Brinkmann, K.; Häger, T.; Hu, T.; Heiderhoff, R.; Shutsko, I.; Görrn, P.; Chen, Y.; et al. Distributed Feedback Lasers Based on MAPbBr3. *Adv. Mater. Technol.* **2018**, *3*, 1700253. [CrossRef]
67. Brenner, P.; Stulz, M.; Kapp, D.; Abzieher, T.; Paetzold, U.W.; Quintilla, A.; Howard, I.A.; Kalt, H.; Lemmer, U. Highly stable solution processed metal-halide perovskite lasers on nanoimprinted distributed feedback structures. *Appl. Phys. Lett.* **2016**, *109*, 141106. [CrossRef]
68. Whitworth, G.L.; Harwell, J.R.; Miller, D.N.; Hedley, G.J.; Zhang, W.; Snaith, H.J.; Turnbull, G.A.; Samuel, I.D.W. Nanoimprinted distributed feedback lasers of solution processed hybrid perovskites. *Opt. Express* **2016**, *24*, 23677–23684. [CrossRef]
69. Schünemann, S.; Brittman, S.; Chen, K.; Garnett, E.C.; Tüysüz, H. Halide Perovskite 3D Photonic Crystals for Distributed Feedback Lasers. *ACS Photonics* **2017**, *4*, 2522–2528. [CrossRef]
70. Wang, K.; Gu, Z.; Liu, S.; Sun, W.; Zhang, N.; Xiao, S.; Song, Q. High-Density and Uniform Lead Halide Perovskite Nanolaser Array on Silicon. *J. Phys. Chem. Lett.* **2016**, *7*, 2549–2555. [CrossRef]
71. Mathies, F.; Brenner, P.; Hernandez-Sosa, G.; Howard, I.A.; Paetzold, U.W.; Lemmer, U. Inkjet-printed perovskite distributed feedback lasers. *Opt. Express* **2018**, *26*, A144–A152. [CrossRef]
72. Bar-On, O.; Brenner, P.; Lemmer, U.; Scheuer, J. Micro Lasers by Scalable Lithography of Metal-Halide Perovskites. *Adv. Mater. Technol.* **2018**, *3*, 1800212. [CrossRef]
73. Zhang, Q.; Sun, H.; Zhang, H.; Jiang, M.; Wu, X.; Zhang, Z.; Yang, T.; Xia, R.; Cabanillas-Gonzalez, J. Facile and Controllable Fabrication of High-Performance Methylammonium Lead Triiodide Films Using Lead Acetate Precursor for Low-Threshold Amplified Spontaneous Emission and Distributed-Feedback Lasers. *Phys. Status Solidi RRL* **2019**, *13*, 1900176. [CrossRef]
74. Gong, J.; Wang, Y.; Liu, S.; Zeng, P.; Yang, X.; Liang, R.; Ou, Q.; Wu, X.; Zhang, S. All-inorganic perovskite-based distributed feedback resonator. *Opt. Express* **2017**, *25*, A1154–A1161. [CrossRef] [PubMed]
75. Chen, S.; Roh, K.; Lee, J.; Chong, W.K.; Lu, Y.; Mathews, N.; Sum, T.C.; Nurmikko, A. A Photonic Crystal Laser from Solution Based Organo-Lead Iodide Perovskite Thin Films. *ACS Nano* **2016**, *10*, 3959–3967. [CrossRef]
76. Li, Z.; Moon, J.; Gharajeh, A.; Haroldson, R.; Hawkins, R.; Hu, W.; Zakhidov, A.; Gu, Q. Room-Temperature Continuous-Wave Operation of Organometal Halide Perovskite Lasers. *ACS Nano* **2018**, *12*, 10968–10976. [CrossRef]
77. Gharajeh, A.; Haroldson, R.; Li, Z.; Moon, J.; Balachandran, B.; Hu, W.; Zakhidov, A.; Gu, Q. Continuous wave operation in directly patterned perovskite distributed feedback light source at room temperature. *Opt. Lett.* **2018**, *43*, 611–614. [CrossRef]
78. Chen, S.; Zhang, C.; Lee, J.; Han, J.; Nurmikko, A. High-Q, Low-Threshold Monolithic Perovskite Thin-Film Vertical-Cavity Lasers. *Adv. Mater.* **2017**, *29*, 1604781. [CrossRef]
79. Huang, C.Y.; Zou, C.; Mao, C.; Corp, K.L.; Yao, Y.C.; Lee, Y.J.; Schlenker, C.W.; Jen, A.K.Y.; Lin, L.Y. CsPbBr3 Perovskite Quantum Dot Vertical Cavity Lasers with Low Threshold and High Stability. *ACS Photonics* **2017**, *4*, 2281–2289. [CrossRef]
80. Wang, J.; Da, P.; Zhang, Z.; Luo, S.; Liao, L.; Sun, Z.; Shen, X.; Wu, S.; Zheng, G.; Chen, Z. Lasing from lead halide perovskite semiconductor microcavity system. *Nanoscale* **2018**, *10*, 10371–10376. [CrossRef]
81. Chen, S.; Nurmikko, A. Stable Green Perovskite Vertical-Cavity Surface-Emitting Lasers on Rigid and Flexible Substrates. *ACS Photonics* **2017**, *4*, 2486–2494. [CrossRef]
82. Chen, S.; Nurmikko, A. Excitonic gain and laser emission from mixed-cation halide perovskite thin films. *Optica* **2018**, *5*, 1141–1149. [CrossRef]
83. Lova, P.; Giusto, P.; Di Stasio, F.; Manfredi, G.; Paternó, G.M.; Cortecchia, D.; Soci, C.; Comoretto, D. All-polymer methylammonium lead iodide perovskite microcavities. *Nanoscale* **2019**, *11*, 8978–8983. [CrossRef] [PubMed]
84. Whitworth, G.L.; Turnbull, G.A. *Organic Lasers with Distributed Feedback: Threshold Minimization and LED Pumping*; Published in Organic Lasers: Fundamentals, Developments, and Applications; Anni, M., Lattante, S., Eds.; Jenny Stanford Publishing: Singapore, 2018; Chapter 7, pp. 285–316.
85. Leyden, M.; Terakawa, S.; Matsushima, T.; Ruan, S.; Goushi, K.; Auffray, M.; Sandanayaka, A.S.D.; Qin, C.; Bencheikh, F.; Adachi, C. Distributed Feedback Lasers and Light-Emitting Diodes Using 1-Naphthylmethylamnonium Low-Dimensional Perovskite. *ACS Photonics* **2019**, *6*, 460–466. [CrossRef]

86. Tessler, N.; Denton, G.J.; Friend, R.H. Lasing from conjugated-polymer microcavities. *Nature* **1996**, *382*, 695–697. [CrossRef]
87. Riechel, S.; Lemmer, U.; Feldmann, J.; Berleb, S.; Mückl, A.G.; Brütting, W.; Gombert, A.; Wittwer, V. Very compact tunable solid-state laser utilizing a thin-film organic semiconductor. *Opt. Lett.* **2001**, *26*, 593–595. [CrossRef] [PubMed]
88. Riedl, T.; Rabe, T.; Johannes, H.H.; Kowalsky, W.; Wang, J.; Weimann, T.; Hinze, P.; Nehls, B.; Farrell, T.; Scherf, U. Tunable organic thin-film laser pumped by an inorganic violet diode laser. *Appl. Phys. Lett.* **2006**, *88*, 241116. [CrossRef]
89. Yang, Y.; Turnbull, G.A.; Samuel, I.D.W. Hybrid optoelectronics: A polymer laser pumped by a nitride light-emitting diode. *Appl. Phys. Lett.* **2008**, *92*, 163306. [CrossRef]
90. Wang, Y.; Morawska, P.O.; Kanibolotsky, A.L.; Skabara, P.J.; Turnbull, G.A.; Samuel, I.D.W. LED pumped polymer laser sensor for explosives. *Laser Photonics Rev.* **2013**, *7*, L71–L76. [CrossRef]